IMPACT OF LOW-LATITUDE IONOSPHERIC DISTURBANCES ON POSITIONING NAVIGATION SYSTEMS AND MACHINE LEARNING IN IONOSPHERIC DISTURBANCE PREDICTION

PHYO C THU

A THESIS SUBMITTED IN PARTIAL FULFILLMENT

OF THE REQUIREMENT FOR THE DEGREE OF

MASTER ENGINEERING IN ELECTRICAL AND COMPUTER ENGINEERIG

SCHOOL OF ENGINEERING

KING MONGKUT'S INSTITUTE OF TECHNOLOGY LADKRABANG

2023

KMITL-2024-EN-M- 027-179

TITLE	Impact of low-latitude ionospheric disturbances on positioning navigation systems and machine learning in ionospheric disturbance prediction
NAME	Phyo C Thu
STUDENT ID	64601010
DEGREE	Master of Engineering
PROGRAME	Electrical and Computer Engineering
ACADEMIC YEAR	2566
THESIS ADVISOR	Prof. Dr. Pornchai Supnithi

ABSTRACT

Equatorial plasma bubbles (EPBs) refer to local ionospheric irregularities or plasma depletions in low-latitude regions at nighttime. They typically originate at the bottom side of the ionosphere and then potentially spread to mid-latitude regions along magnetic field lines. With precise positioning and navigation techniques becoming increasingly crucial to various segments of society, it is importantl to be aware of and investigate the performance degradation of these systems caused by EPBs at low latitudes. In this work, we analyze the effects of EPBs on the performance of real-time kinematic (RTK) positioning at low-latitude stations in Thailand in 2020 (solar minimum) and 2022 (ascending phase to solar maximum). We particularly highlight the relationship between positioning errors and baseline lengths. The results show that the positioning errors are 2 times higher during disturbance periods and especially, 5 times more severe in long baselines compared with shorter ones, especially during the equinoctial periods. In addition, we examine the performance of RTK with a long baseline at different latitude regions in Thailand. Similarly, we also examine the effects of EPBs over ionospheric delay gradients for ground-based augmentation (GBAS) near the Suvarnabhumi International Airport. We observe that the EPBs cause very large ionospheric delay gradients in all affected satellite signals at all elevation angles during disturbed time compared to the occurrence of large gradients (lower than gradient caused by EPBs) at low elevation angles. In addition, we propose a machine learning technique to predict the movement of EPBs by convolutional long short-term memory (LSTM) model with next-frame prediction approach using the ionospheric ROTI map of Thailand region. The proposed model shows the applicability and feasibility of machine learning approach in EPB prediction with relatively low errors.

ACKNOWLEDGEMENTS

This Master thesis is financially supported by King Mongkut's Institute of Technology Research Fund (Grant no. KREF016422), ASEAN IVO (http://www.nict.go.jp/en/asean_ivo/index.html) project, [Research and development for precise positioning with Artificial Intelligence (AI) during ionospheric disturbances in low-latitude region in ASEAN], and NSRF via the Program Management Unit for the Human Resources & Institutional Development, Research and Innovation (grant no. B05F640197). My heartfelt appreciation goes to my dedicated supervisor, Prof. Dr. Pornchai Supnithi from King Mongkut's Institute of Technology Ladkrabang, whose unwavering support and guidance have been the driving force behind this meaningful journey of my graduate study. I am also deeply grateful to Asst. Prof. Dr. Lin Min Min Myint and Dr. Jirapoom Budtho from King Mongkut's Institute of Technology Ladkrabang, as well as Dr. Susumu Saito from Electronic Navigation Research Institute, Japan, for their invaluable advice and guidance throughout my research. Furthermore, I wish to extend my thanks to all the members of the Excellence Center in Thai GNSS and Space Weather Information Data Center, whose support has been instrumental in the success of my thesis.

Moreover, I am thankful to the Thai GNSS and Space Weather Information Data Center for the GPS data and processing program, Stamford International University, Aeronautical Radio of Thailand, Department of Land Thailand, Department of Public Works and Town & Planning Thailand and Royal Thai Survey Department for providing the GNSS data, National Institute of Communication Technology (Japan) and Electronics Navigation Research Institute (Japan) for providing the GNSS observation equipment.

Finally, I am thankful to the committee members who assessed my Master thesis during the defense. Your expert questions and comments added important technical and scientific dimensions to this work.

Phyo C Thu

TABLE OF CONTENTS

LIST OF FIGURES

LIST OF TABLES

ABBREVIATIONS

RTK	Real-time Kinematic
EPB	Equatorial Plasma Bubble
TEC	Total Electron Content
STEC	Slant Total Electron Content
AATR	Along the Arc TEC Rate
ROTI	Rate of TEC Change Index
Kp	Planetary K-index
Dst	Disturbance Storm Time Index
VHF	Very High Frequency
DOY	Day of Year
GNSS	Global Navigation Satellite System
GPS	Global Positioning System
SD	Single Difference
DD	Double Difference
LAMBDA	Least-Squares Ambiguity Decorrelation
ILS	Inter Lease Square
ECEF	Earth-centered, Earth-fixed coordinate system
RTKLIB	Open-source RTK processing software library
HPE	Horizontal Positioning Error
VPE	Vertical Positioning Error
GBAS	Ground-based Augmentation System
SF-CBCA	Single frequency carrier-based code aided
LSTM	Long Short-Term Memory
LSWS	Large scale wave structure
MATLAB	Matrix laboratory
MSE	Mean square error
SSIM	Structural similarity sndex
IRI	International reference ionosphere
Numpy	Python programming language library

Chapter 1 Introduction

1.1 Statement of the problems

Global Navigation Satellite System (GNSS) is an ensemble of satellite navigation systems in which earth-orbiting GNSS satellites, ground control stations, and receivers jointly operate and serve as critical positioning, navigation and timing (PNT) infrastructure. Numerous factors that affect the GNSS positioning accuracy are, for example, satellite and receiver clock offsets, satellite and receiver biases, pseudorange errors, multipath and delays in the ionosphere and troposphere [1], [2]. Despite being one of the most significant sources of ranging errors, the ionospheric delay can be estimated and partially corrected. [3], particularly using the well-known Klobuchar models such as GPS Klobuchar (GPSKlob), BDS Klobuchar (BDSKlob) and NeQuick Galileo (NeQuickG) for single-frequency users [4]–[6] as well as ionospheric-free combination when multiple frequencies are available [7].

The ionosphere is one of the layers of the Earth's atmosphere that extends from 50 km to 1000 km above the surface of the planet. It is ionized by solar and cosmic radiations [8]. The electron density in the ionosphere is a well-known parameter for describing ionospheric conditions. The electron density varies on a diurnal (daytime, nighttime), seasonal (equinox, solstices), and annual (solar activity) basis. Typically, the Total Electron Content (TEC) electron density is higher during the day and lower at night.

Importantly, post-sunset ionospheric disturbances known as equatorial plasma bubbles (EPB) commonly occur at the magnetic equator and in low-latitude regions [9]–[11]. Previous works have extensively studied EPB characteristics [1], [12], [13]. For example, the typical longitudinal width of EPB is about 100 km, and the latitudinal extent can be up to several thousand km [1]. EPBs usually grow vertically and elongate along the field lines to latitudes from the equator [13]. EPB can cause signal fading and high scintillation intensity, leading to performance degradation in positioning and navigation [12].

A number of prior works have examined the negative effects of global ionospheric disturbances on the GNSS precise positioning system during storm events [14]–[17]. The study conducted in Greenland during the St. Patrick's Day storm observed a significant effect of ionospheric disturbances on the integer ambiguity resolution, significantly degrading the accuracy of float RTK positioning and a minor decrease in float solution accuracy during the disturbed period [14]. The global study conducted during the 2015 St. Patrick's Day geomagnetic storms reveals a

severe degradation of PPP positioning accuracy at high latitudes of up to 10 m and a moderate degradation of PPP performances at mid-latitudes of up to 2 m [15]. The study on the Norwegian RTK Network in high attitude regions also presents increments of positioning errors exponentially with ROTI [16]. The meter-level degradation of precise positioning accuracy in the American sector multi-site GNSS network is also caused by storm-induced equatorial plasma bubbles [17]. In addition, the statistically positive strong correlation between ionospheric disturbance and GNSS positioning is also discussed based on observation data from 2012 in high-latitude regions [3].

Few studies have emphasized the effects of ionospheric disturbances in low-latitudes on high-accuracy positioning[18]–[20]. The study on the impact of ionospheric irregularities over kinematic PPP in the China region during geo storms and global activities observed the meter-level accuracy during disturbed time compared to centimeter-level during quiet time[20]. Another study in China covering low and mid-latitude regions highlights the increments of kinematic PPP errors during storm days [19]. Moreover, the study in Hong Kong during solar maximum of 2014 presents the occurrence of PPP accuracy degradation during high scintillation intensity due to ionospheric disturbance[18].

In addition, those ionospheric irregularities also have effect on aeronautical navigation system such as ground-based augmentation system (GBAS) used for aircraft landing approaches due to occurrence of large ionospheric delay gradient [1]. The ionospheric delay gradient is the spatial difference in the ionospheric delay [21] and usually described unit of mm/km [22]. In GBAS, normally occurring gradients are mitigated by determining a conservative one-sigma parameter. However, abnormal large gradients caused by ionospheric disturbance such as EPB need to be monitored to create ionospheric threat model.

Since EPBs can significantly impact the positioning and navigation systems, various approaches, particularly with AI, have been applied to forecast the ionosphere and EPBs [23]–[25]. In[23] , bidirectional Long Short-Term Memory (LSTM) method has been applied to create the Ionospheric TEC 2-hour prediction maps based on the observation data of 257 stations over China region. There is also another approach for prediction of EPB by using the SWARM satellite data with random forest aggressor [24]. However, there is limitation with SWARM data due to limited number of satellites. Another approach for prediction of ionospheric disturbances based on GNSS ROTI map has been studies in high-latitude region using machine learning approach [25].

Since Thailand is located on the magnetic equator, where frequent and severe occurrences of EPB are seen, especially during the approaching solar maximum, it is an ideal location to perform the study on EPBs. Therefore, this thesis focuses on studying effects of EPBs over RTK positioning

system as well as the impact over ionospheric delay gradient for GBAS. We also discus development of machine learning approach for forecasting of EPB over Thailand region.

1.2 Objectives

In this thesis, there are three main objectives as follows.

(a) To study the impact of EPBs over real-time kinematic positioning system in Thailand region
(b) To study the impact of EPBs over ionospheric delay gradients for GBAS in Thailand region
(c) To develop machine learning models for low-latitude ionospheric disturbance prediction

1.3 Scope of the study

In this work, we mainly focus on the impact of EPBs on positioning and navigation systems. The scope of this study is separated into three separate works.

Firstly, to study the impacts of EPBs over RTK positioning system, we analyze the performances of RTK positioning in the Bangkok area in 2020, the solar minimum phase of solar cycle #25, and 2022, the ascending phase of solar cycle #25. The experiments at the short, medium, and long baselines by RTK based on GPS L1 frequency postprocessing are performed, and latitudinal RTK positioning performance is also presented. We present the summarized statistics of RTK positioning performance from conducted experiments and highlight the relationship between ROTI and RTK positioning performance.

Secondly, we study the impact of ionospheric irregularities over ionospheric delay gradients for GBAS in Thailand region. We analyze the ionospheric delay gradients for GBAS using observation data of 2021 from three stations located around the Suvarnabhumi International airport. We compare the behavior of ionospheric delay gradient during quiet days and disturbed days with EPBs occurrences.

Finally, we develop a machine learning model to predict low-latitude ionospheric disturbances. We propose a machine learning technique to predict the movement of EPBs by a convolutional long short-term memory (LSTM) model with next-frame prediction approach using the ionospheric ROTI map as one of the inputs. We present the performance of our proposed model by comparing the prediction with actual ROTI maps.

1.4 Thesis outlines

This thesis is categorized into six chapters. In Chapter 1, motivation of this work, objectives, scope of this works, and outlines of the thesis are discussed.

In Chapter 2, we present the related theories for this study. First, ionosphere and ionospheric parameters are explained. After that the related theories to perform the RTK positioning are explained in detail. Theories about ground-based augmentation system (GBAS) and computation of ionospheric delay gradient are also presented in this chapter. The basics theories about convolutional LSTM model for next frame prediction are also expressed in chapter.

In Chapter 3, we discuss the experimental setups for this study. The experimental setups for studying the impact of EPBs on RTK positioning and ionospheric delay gradients for GBAS are presented in this chapter. In addition, we discuss the data-preprocessing and the architecture of the proposed convolutional LSM model presented in this chapter.

In Chapter 4, we present the results of the conducted experiments. We present the RTK positioning performances at various baseline lengths as well as at different latitudes and the statistics of RTK positioning performance in 2020 and 2022. In addition, the impact of ionospheric delay gradients for GBAS is analyzed in Thailand. The performance of the proposed convolutional LSTM model is presented in this chapter.

In chapter 5, we summarize all the works included in this thesis and discuss the extended works in the future.

Chapter 2 Background theories

In this chapter, we will discuss the background theories related to ionospheric study, real-time kinematic positioning system, ground-based augmentation system and as well as convolutional LSTM model which will be used for studying the application of machine learning approach in ionospheric disturbance prediction.

2.1 Ionospheric parameters and equatorial plasma bubbles

2.1.1 Ionosphere and equatorial plasma bubbles (EPB)

The electron density in the ionosphere varies with time, location, solar and geomagnetic activities [26]. Local ionospheric disturbances at low-latitude regions are caused by both global disturbed conditions as well as local conditions. However, weak global disturbances do not always cause disturbances in the local ionosphere. The earth's global geomagnetic activity is generally measured in planetary K-Index (Kp) and disturbance storm time (Dst) index. For magnetic equator and low-latitude region, local ionospheric irregularity known as equatorial plasma bubbles (EPB) are common [1].

EPBs refer to plasma depletion surrounded by background (relatively higher) electron density, hence, having the shape similar to bubbles. They occur at the bottom side of the F layer due to Rayleigh-Taylor instability [27] after sunset, then potentially spread to higher latitudes along the magnetic field lines [28]. When it evolves to the higher altitude, it potentially spreads to the higher latitudes along the magnetic field lines [28]. Due to the ionospheric irregularities in EPB, ionospheric delay can fluctuate the measurement of GNSS signals [1]. EPBs can, however, be caused by global disturbances due to high solar activities; therefore, they appear more frequently during high solar periods than low solar periods [29]. EPBs can be observed through various methods including VHF radar stations, in situ satellite measurements, all-sky imagers, ground based GNSS receivers [30]. The example of EPB observed by using equatorial plasma bubbles using VHF radar station is shown in Figure 2.1. The example of EPB observed by ROTI map of ground based GNSS receiver on DOY 044, 2023 is also shown in Figure 2.2.

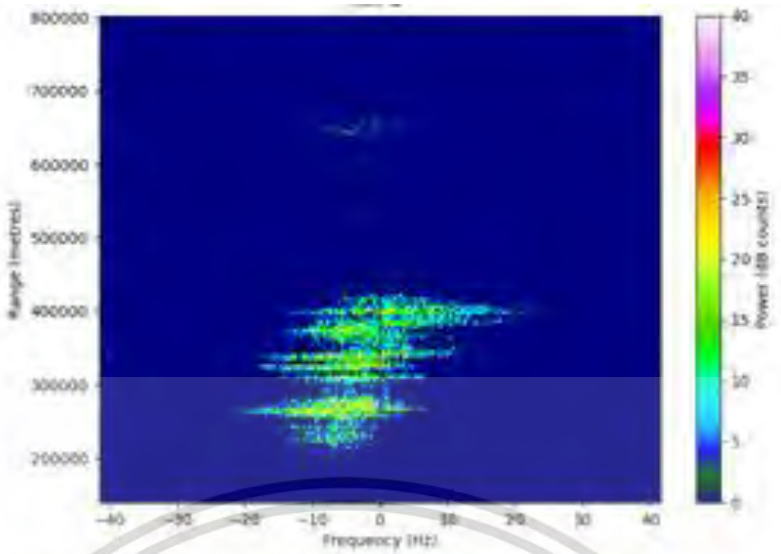

Figure 2.1 EPB observed from Chumpom VHF radar station on October 13, 2020.

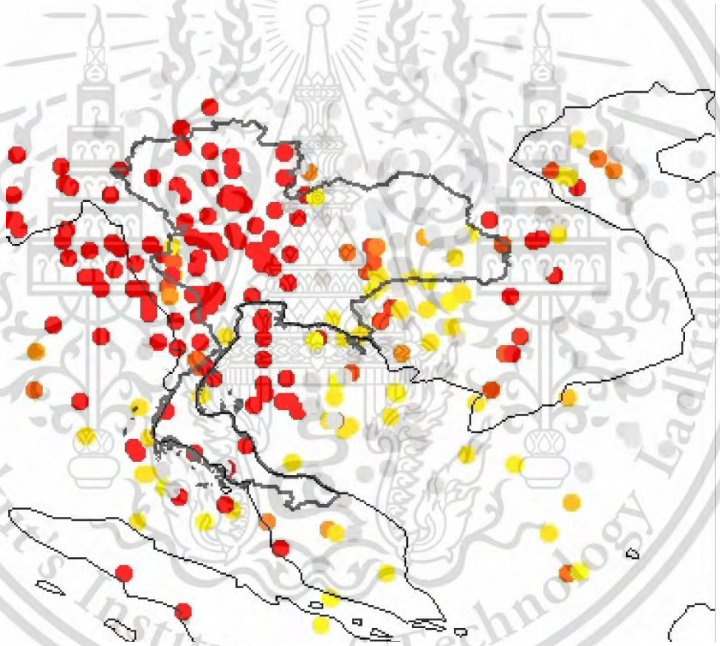

Figure 2.2 EPB observed by ground based GNSS receivers on DOY 044, 2023.

2.1.2 Total electron content (TEC)

Total electron content (TEC) is used to describe the electron density in ionosphere and be computed from the two GPS signals of f1 = 1575.42 MHz and f2 = 1227.60 MHz frequencies. The slant Total Electron Content (STEC) is defined as the density of electrons along the line-of-sight path between a satellite and a receiver in the ionosphere layer[31] as shown in Figure 2.3. At a single location, the STEC varies due to elevation angles of satellites as well as the time of day. To compute the STEC, we employ the geometric-free combination of code and carrier phase pseudorange of two frequencies, in GPS, can be used. [12]

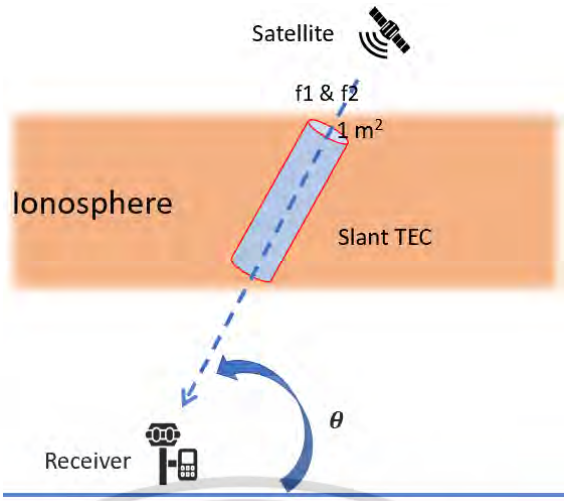

Figure 2.3 Slant Total Electron Content (STEC)

Based on GPS signals, STEC can be obtained from the difference between the pseudorange (P_1 and P_2), $STEC_P$, and the difference between the carrier phases (L_1 and L_2), $STEC_L$, of the dual L-band frequencies [32], i.e.,

$$STEC_p = \frac{2 f_1^2 f_2^2}{k(f_1^2 - f_2^2)}(P_2 - P_1), \quad 2.1$$

and

$$STEC_L = \frac{2 f_1^2 f_2^2}{k(f_1^2 - f_2^2)}(L_1\lambda_1 - L_2\lambda_2), \quad 2.2$$

where k is related to ionospheric refraction (80.62 m^3/s^2), f_1 = 1575.42 MHz, and f_2 = 1227.60 MHz, and λ_1 and λ_2 are the wavelengths with respect to f_1 and f_2, respectively. An example of raw STEC from code pseudorange measurement of the KMIT observation station on DOY 001, 2020 is shown in Figure 2.4. Similarly, Figure 2.5 shows the raw STEC from carrier phase measurements of the KMIT station on the same day.

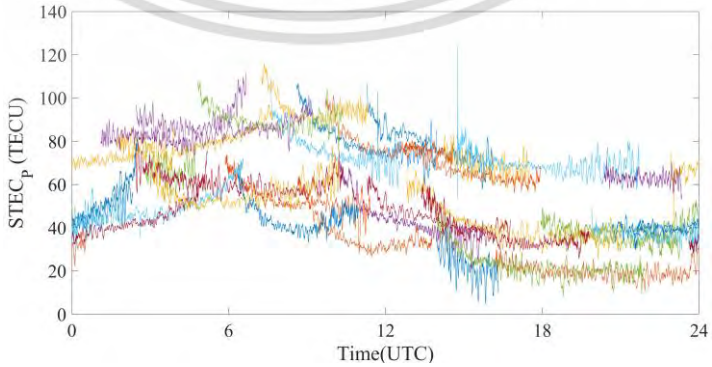

Figure 2.4 Example of raw STEC from code pseudorange of KMIT observation station at DOY 001, 2021.

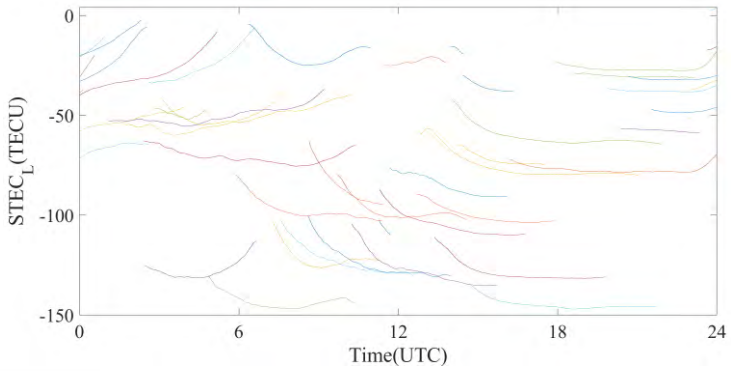

Figure 2.5 Example of raw STEC from the carrier-phase measurement of KMIT observation station at DOY 001, 2021.

As we can see in Figure 2.4 and Figure 2.5 , the levels of STEC from code pseudorange ($STEC_P$) are relatively noisy while the variations of STEC from carrier-phase ($STEC_L$) are smooth. In general, $STEC_L$ is more precise, smoother, and less sensitive to multipath than $STEC_P$, although it contains integer ambiguity due to cycle slip issue The $STEC_L$ is then adjusted to the $STEC_P$ levels with phase leveling [33], to obtain adjusted STEC, $STEC_{adj}$,i.e.,

$$STEC_{adj} = STEC_L + \overline{STEC_P - STEC_L}, \quad 2.3$$

where $\overline{STEC_P - STEC_L}$ is the mean of the difference between $STEC_P$ and $STEC_L$. An example of the adjusted STEC after phase leveling on DOY 001,2021 is shown in Figure 2.6.

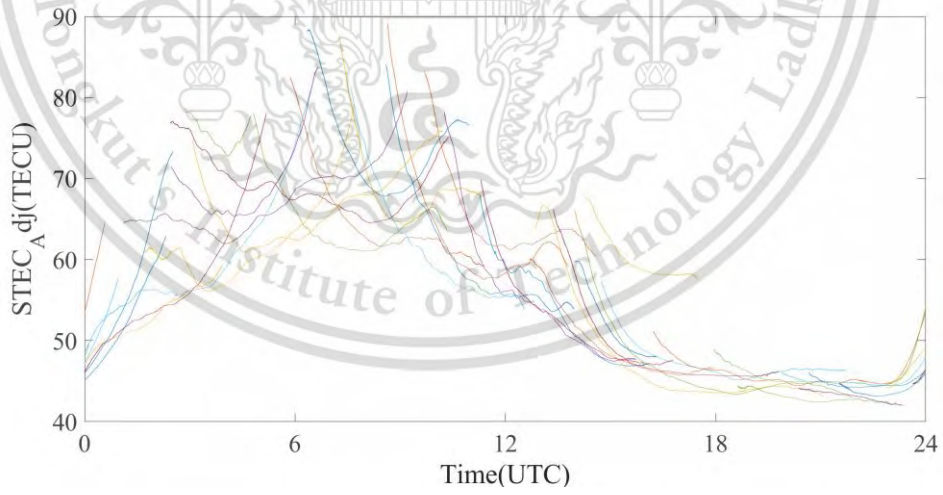

Figure 2.6 Example of carrier-phase STEC after leveling to code-STEC at KMIT station on DOY 001, 2021.

The STEC can then be converted to vertical total electron content (VTEC) which is the density of electrons in the ionosphere along the vertical path as shown in Figure 2.7. VTEC can be calculated

by multiplying with the slant factor with respect to the elevation angles of satellites based on the Single Layer Ionospheric Model (SLIM) [34], i.e.,

$$VTEC = STEC_{adj} \cos x \,, \tag{2.4}$$

where $cosx$ is the slant factor related to elevation angles of GPS satellites which can be computed from

$$\cos x = \sqrt{1-(\frac{R_E}{R_E + h_{iono}}\cos\theta)^2} \,, \tag{2.5}$$

where R_E is the radius of the earth (6,378,137 meters in WGS84 standard), h_{iono} is the assumed height of the ionosphere at 350 km and θ is the elevation angle of the satellite as shown in Figure 2.7.

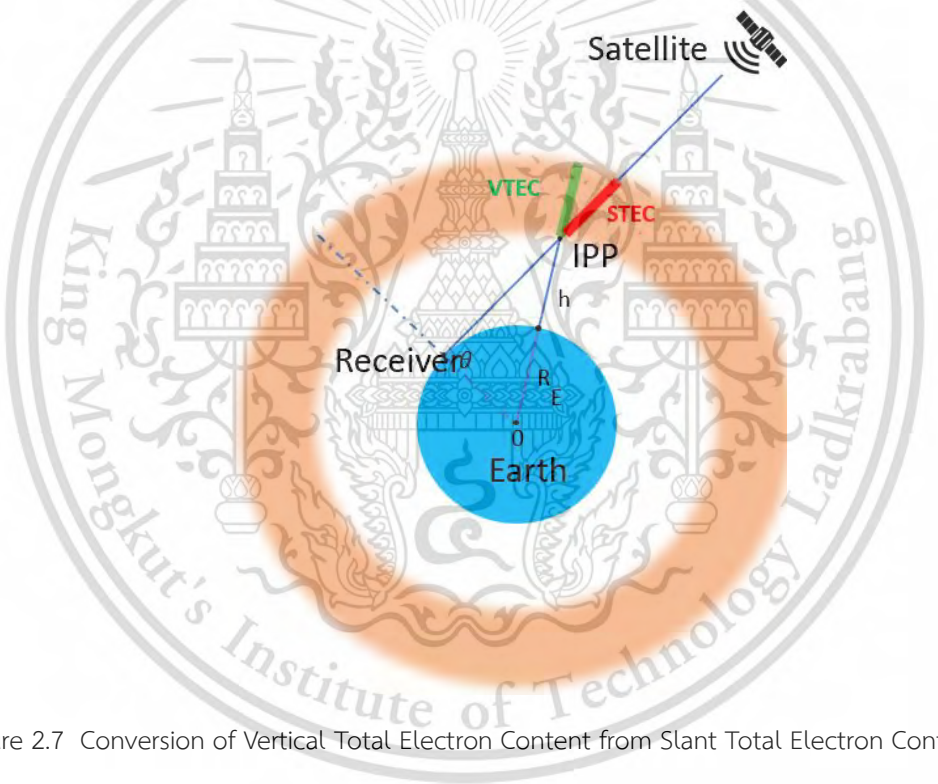

Figure 2.7 Conversion of Vertical Total Electron Content from Slant Total Electron Content based on SLIM

Since, in reality, the STEC contains inherent delays from satellite bias and receiver bias as discussed in the previous section, the VTEC without instrumental satellite bias and receiver bias can be expressed as

$$VTEC = (STEC_{adj} - B_s - B_r)\cos x \,, \tag{2.6}$$

where B_s is the satellite bias and B_r is the receiver bias. The satellite bias of the GPS satellites can be obtained from International GNSS Service (IGS) by CODE (Center of Orbit Determination in Europe)

[35] and the receiver bias still needs to be estimated based on these computed adjusted STEC from (3) after removing the satellite bias.

The minimum standard deviation method [32] is a well-known approach to estimate the receiver bias of a single receiver. In this method, the receiver bias is derived after the satellite bias is removed from the adjusted STEC. It is assumed that the VTEC with the low elevation angle should not be different from the VTEC computed from high elevation angles since VTEC is computed from the GPS observation of all satellites. The sum of the standard deviation of VTEC (σ_{Total}) will be minimized when we select the appropriate receiver bias. It can be computed from (σ_{Total}) [36], i.e.,

$$\sigma_{Total} = \sum_{j=1}^{N_t} \sigma_{VTEC,j} , \qquad 2.7$$

where N_t is the number of satellites at the same time and standard deviation of VTEC (σ_{VTEC}) is

$$\sigma_{VTEC,j} = \sqrt{\frac{1}{N_{sat,j}} \sum_{i=1}^{N_{sat,j}} (VTEC_{j,i} - \overline{VTEC_j})^2} , \qquad 2.8$$

where $N_{sat,j}$ is the number of satellites at time j, $VTEC_{j,i}$ is the VTEC of the i^{th} satellite at time j and $\overline{VTEC_j}$ is the mean of the VTEC of visible satellites at time j.

To estimate the receiver bias, various receiver bias values are applied for converting the STEC to VTEC with respect to equation 2.6. After that, the standard deviation of the VTEC is computed and the receiver bias value which can give the minimum standard deviation of VTEC is assumed to be the correct receiver bias based on equations 2.7 and 2.8. An example of VTEC after removing receiver bias is shown in Figure 2.8.

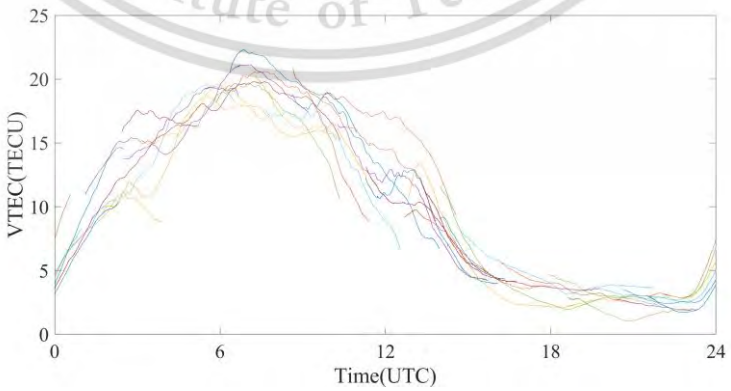

Figure 2.8 Example of VTEC after removing the instrumental bias (satellite and receiver bias) of the KMIT observation station on DOY 001, 2021.

2.1.3 Rate of TEC change index (ROTI)

One of the parameters to determine the local ionospheric disturbances is the rate of TEC change index (ROTI) [37]. ROTI is the standard deviation of the rate of TEC (ROT) during an interval of time, generally in the 5-min time intervals. The ROTI index can be expressed [3] as

$$ROTI = \sqrt{\frac{1}{N}\sum_{i=1}^{N}(ROT(i) - \overline{ROT})^2}\ , \qquad 2.9$$

where ROT is the difference in slant total electron content (STEC) during a time interval which can be obtained from

$$ROT = (STEC(i+1) - STEC(i))\,, \qquad 2.10$$

where $STEC(i+1)$ and the $STEC(i)$ denotes STEC at epochs *i*+1 and *i,* respectively. STEC can be computed from a linear combination of dual-frequency GNSS receiver. An example of ROTI plot on October 3,2022 at KMIT station from Thailand is shown in Figure 2.9. The ROTI levels are very high from 12:00 to 18:00 UTC (19:00 to 03:00 LT). High ROTI indicates the fluctuation in TEC caused by ionospheric disturbance possibly by EPBs.

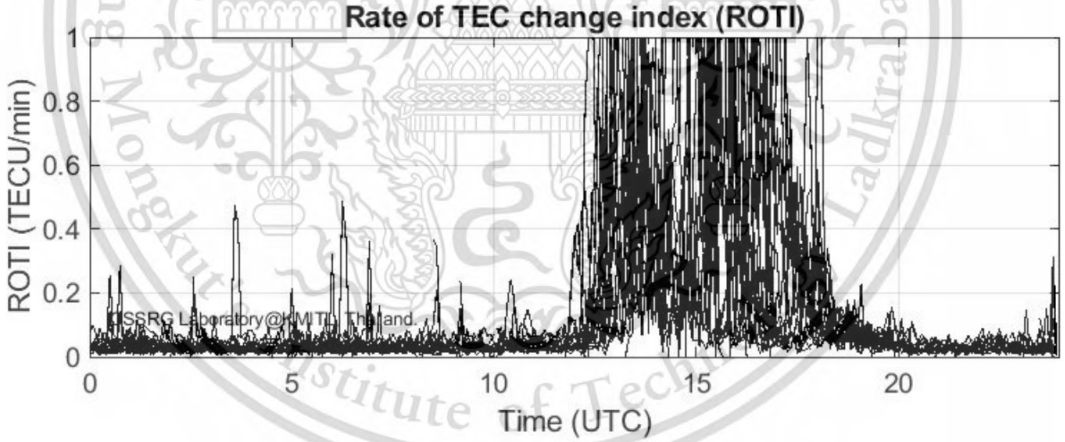

Figure 2.9 Example of ROTI at KMIT station in October 3, 2022.

2.1.4 Along the arc TEC rate (AATR)

Along the arc TEC rate (AATR), is also another ionospheric index to determine whether the ionospheric activity is disturbed or quiet. AATR is computed from STEC of carrier phase. the variation of the STEC between two consecutive observations separated Δt, can be computed for a given epoch, t, [38] as

$$\Delta STEC_{t}\ j(t) = LI_i^j(t) - LI_i^j(t - \Delta t)\,, \qquad 2.11$$

where i denotes the receiver, j is the satellite number, and LI is the geometry-free combination of carrier phase.

After that AATR is computed as [38],

$$AATR_i^j(t) = \frac{1}{(M(\varepsilon))^2} \times \frac{\Delta STEC_i^j(t)}{\Delta t}, \quad 2.12$$

where Δt is the sampling rate of the carrier-phase measurement and $M(\varepsilon)$ is an obliquity, or slant factor defined as the secant of the zenith angle at the mean ionospheric height, that is typically assumed at a 350 km of attitude. $M(\varepsilon)$ projects the vertical to slant delay in a thin-shell model of the ionosphere and only depends on the satellite elevation angle ε. The rapid increase in AATR indicates the ionosphere irregularities.

2.1.5 Global indices in space weather

The Kp-index is used to describe the disturbances of the Earth's magnetic field caused by the solar wind [39]. **Kp** is the mean standardized K-index from 13 geomagnetic observatories between 44 degrees and 60 degrees northern or southern geomagnetic latitude. The **K-index** is quasi-logarithmic local index of the 3-hourly range in magnetic activity relative to an assumed quiet-day curve for a single geomagnetic observatory site. The Kp-index ranges from 0 to 9 indicating from lowest to highest geomagnetic activity although recently, the decimal Kp are also provided [39]. The Kp-index above 5 typically indicates geomagnetic storms. An example of Kp-index from "Space Weather Live" [40] on October 3, 2022, is shown in Figure 2.10.

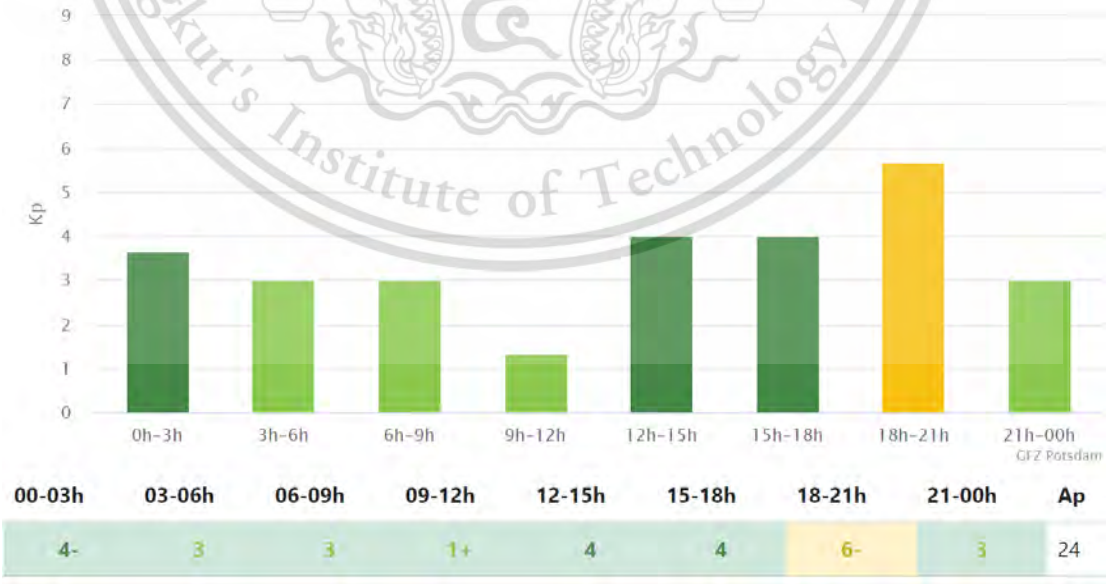

Figure 2.10 An example of Kp-index on October 3, 2022 [41].

The disturbance storm time (Dst) index is a measure that gives information on the strength of the ring current around Earth caused by solar protons and electrons [42]. An example of Dst-index in November 2022 [41] is shown in Figure 2.11. Values between -50 nanotesla (nT) and -100 nanotesla (nT) indicate moderate geomagnetic activities and value less than -100 nT indicate strong geomagnetic activities as we can see in November 7, 2022.

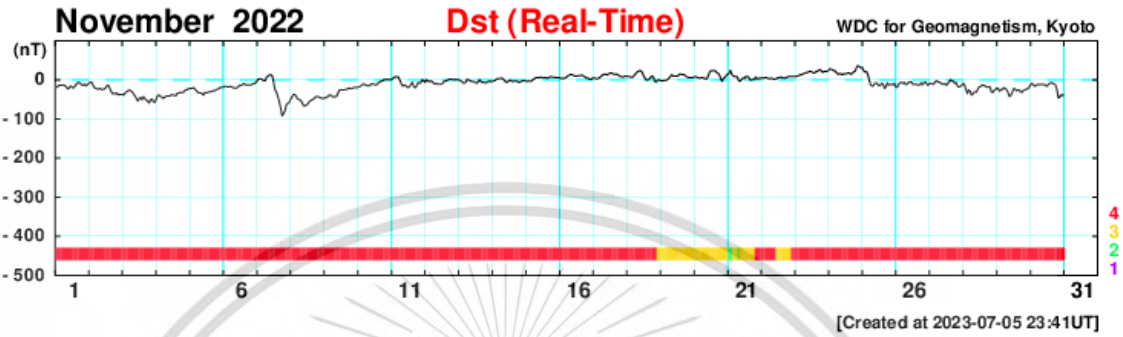

Figure 2.11 An example of Dst-index in October 2022 [41] .

2.2 Real-time kinematic (RTK) positioning system

In this work, we study the impact of low-latitude ionospheric disturbance such as EPBs over the real-time kinematic (RTK) positioning technology. RTK positioning enables centimeter-level accuracy positioning by using the satellite signal's carrier phase, and it is widely employed in today's vital technologies such as surveying, construction, precise agriculture, auto-drive/autopilot vehicle systems [43]–[45]. The RTK technology employs ambiguity resolution and differential correction technique. The rover stations (users) determine their positions with the error corrections received from a base station or a Continuously Operating Reference Station (CORS) network as shown in Figure 2.12.

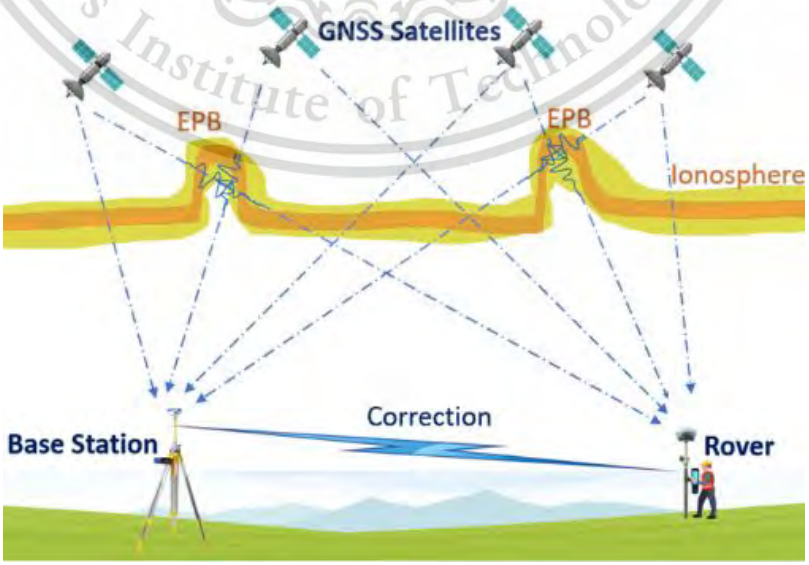

Figure 2.12 An example of RTK system.

In this work, we use opensource software called “RTKLIB” to perform RTK positioning. The mathematical model [46] for RTK positioning by “RTKLIB” can be processed as shown in Figure 2.13.

Figure 2.13 RTK positioning procedure for rover’s positioning computation

Single difference (SD) and double difference (DD) are computed from measurement data of base and rover station as shown in Figure 2.14.

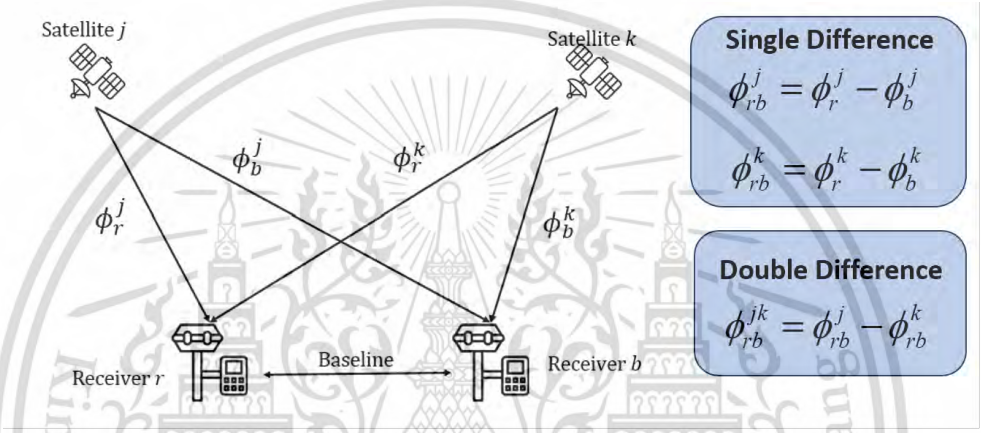

Figure 2.14 SD and DD measurement models for base and rover.

The carrier-phase measurements at a base station with frequency band i can be from satellite j and k as express by

$$\phi_b^j = R_b^j + c(\Delta t_b - \Delta T^j) - I_{i,b}^j + T_b^j + \lambda_i N_{i,b}^j + \varepsilon_{\phi,b}^j , \quad 2.13$$

$$\phi_b^k = R_b^k + c(\Delta t_b - \Delta T^k) - I_{i,b}^k + T_b^k + \lambda_i N_{i,b}^k + \varepsilon_{\phi,b}^k , \quad 2.14$$

where ϕ is the carrier-phase measurement R is the actual geometric range, I is the ionospheric delay, T is the tropospheric delay, N is the carrier -phase ambiguity, ΔT is the satellite clock error, Δt is the receiver clock error, and ε is the measurement noise.

Similarly, the carrier -phase measurement of rover station with frequency band i from satellite j and k can be express as

$$\phi_r^j = R_r^j + c(\Delta t_r - \Delta T^j) - I_{i,r}^j + T_r^j + \lambda_i N_{i,r}^j + \varepsilon_{\phi,r}^j , \quad 2.15$$

$$\phi_r^k = R_r^k + c(\Delta t_r - \Delta T^k) - I_{i,r}^k + T_r^k + \lambda_i N_{i,r}^k + \varepsilon_{\phi,r}^k . \quad 2.16$$

2.2.1 Single difference (SD) combination

As shown in Figure 2.14, the single difference of base and rover from satellite *j* can be computed from equations 2.13 to 2.14 in order to remove the satellite clock error as

$$\begin{aligned}\phi_{rb}^{j} &= \phi_{r}^{j} - \phi_{b}^{j} \\ &= R_{r}^{j} + c(\Delta t_{r} - \Delta T^{j}) - I_{i,r}^{j} + T_{r}^{j} + \lambda_{i} N_{i,r}^{j} + \varepsilon_{\phi,r}^{j} \\ &\quad -(R_{b}^{j} + c(\Delta t_{b} - \Delta T^{j}) - I_{i,b}^{j} + T_{b}^{j} + \lambda_{i} N_{i,b}^{j} + \varepsilon_{\phi,b}^{j}) \\ &= (R_{r}^{j} - R_{b}^{j}) + c(\Delta t_{r} - \Delta t_{b}) - (I_{i,r}^{j} - I_{i,b}^{j}) + (T_{r}^{j} - T_{b}^{j}) \\ &\quad \lambda_{i}(N_{i,r}^{j} - N_{i,b}^{j}) + (\varepsilon_{\phi,r}^{j} - \varepsilon_{\phi,b}^{j})\end{aligned} \quad . \qquad 2.17$$

Assuming that a rover and base station are located in same region, ionospheric and tropospheric delay are considered similar, i.e.,

$$(I_{i,r}^{j} - I_{i,b}^{j}) + (T_{r}^{j} - T_{b}^{j}) \approx 0 \, . \qquad 2.18$$

Given that $R_{rb}^{j} = R_{r}^{j} - R_{b}^{j}$, $N_{i,rb}^{j} = N_{i,r}^{j} - N_{i,b}^{j}$ and $\varepsilon_{\phi,rb}^{j} = \varepsilon_{\phi,r}^{j} - \varepsilon_{\phi,b}^{j}$, equation 2.17 can be rewritten as

$$\phi_{rb}^{i} = R_{rb}^{j} + c(\Delta t_{r} - \Delta t_{b}) + \lambda_{i} N_{i,rb}^{j} + \varepsilon_{\phi,rb}^{j} \, . \qquad 2.19$$

Similarly, the single difference (SD) measurement for satellite *k* can be expressed as

$$\phi_{rb}^{k} = R_{rb}^{k} + c(\Delta t_{r} - \Delta t_{b}) + \lambda_{i} N_{i,rb}^{k} + \varepsilon_{\phi,rb}^{k} \, . \qquad 2.20$$

2.2.2 Double difference (DD) combination

As shown in Figure 2.14, the double difference measurement (DD) can be computed from SD from equations 2.19 and 2.20 to eliminate the receiver clock error as

$$\begin{aligned}\phi_{rb}^{jk} &= \phi_{rb}^{j} - \phi_{rb}^{k} \\ &= R_{rb}^{j} + c(\Delta t_{r} - \Delta t_{b}) + \lambda_{i} N_{i,rb}^{j} + \varepsilon_{\phi,rb}^{j} \\ &\quad -(R_{rb}^{k} + c(\Delta t_{r} - \Delta t_{b}) + \lambda_{i} N_{i,rb}^{k} + \varepsilon_{\phi,rb}^{k}) \\ &= (R_{rb}^{j} - R_{rb}^{k}) + \lambda_{i}(N_{i,rb}^{j} - N_{i,rb}^{k}) + (\varepsilon_{\phi,rb}^{j} - \varepsilon_{\phi,rb}^{k})\end{aligned} \quad . \qquad 2.21$$

Given that $R_{rb}^{jk} = R_{rb}^{j} - R_{rb}^{k}$, $N_{i,rb}^{jk} = N_{i,rb}^{j} - N_{i,rb}^{k}$, and $\varepsilon_{\phi,rb}^{jk} = \varepsilon_{\phi,rb}^{j} - \varepsilon_{\phi,rb}^{k}$, equation 2.21 can be rewritten as

$$\phi_{rb}^{jk} = R_{rb}^{jk} + \lambda_i N_{i,rb}^{jk} + \varepsilon_{\phi,rb}^{jk} . \quad 2.22$$

The double difference measurement (DD) for code-psudorange can be expressed similarly as

$$\rho_{rb}^{jk} = R_{rb}^{jk} + \varepsilon_{\rho,rb}^{jk} . \quad 2.23$$

From equations2.22 and 2.23 , rover position is estimated by using Kalman Filter.

2.2.3 Rover position computation using Kalman filter

Firstly, we will discuss the Kalman filter for RTK positioning estimation process as shown in Figure 2.15.

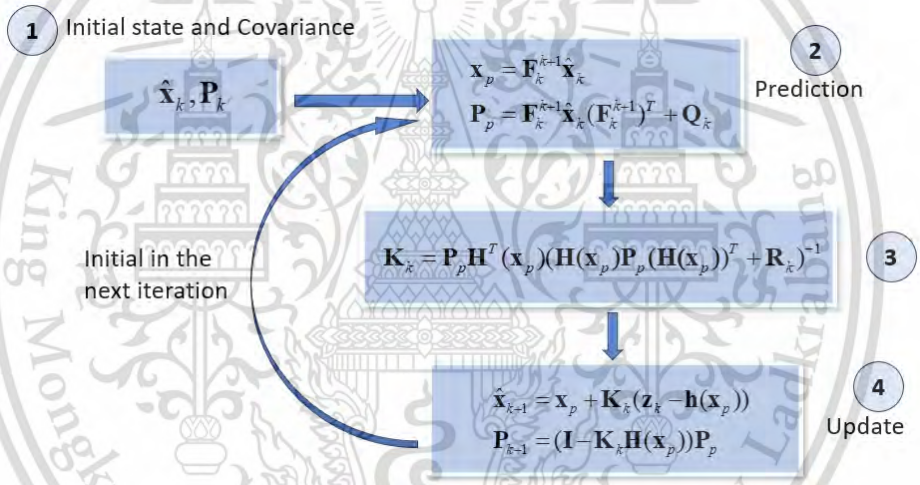

Figure 2.15 Steps of Kalman Filter for RTK positioning

As shown in Figure 2.15, Kalman filter works in 4 steps as follows.

1) Define the state vector and covariance matrix at time k , $\hat{\mathbf{x}}_k$ and $\mathbf{P}_k$ with default values where

$$\mathbf{P}_k = E\{(\hat{\mathbf{x}}_k - \hat{\mathbf{x}}_{k+1}) + (\hat{\mathbf{x}}_k - \hat{\mathbf{x}}_{k+1})^T\} , \quad 2.24$$

where $\mathbf{P}_k$ is the error covariance matrix from estimation.

2) Predict the state vectors and covariance matrix using the equation of $\mathbf{F}_k^{k+1}$

3) Calculate the Kalman Filter gain $\mathbf{K}_k$ from measurement covariance $\mathbf{R}_k$ and predict the covariance

4) Repeat the prediction from step 1 with gain $\mathbf{K}_k$ with the measured value vector $\mathbf{z}_k$

Then, the output from step 4 becomes the input of step 1 of the cycle calculation. Afterwards, iterative calculations are performed following these steps until the accurate output is obtained. Parameters for the Kalman filter used in RTK positioning are shown in Table 2.1.

Table 2.1 Parameters for Kalman filter used in RTK positioning

Parameter	Matrix/Vector Size	Description
$\hat{\mathbf{x}}_k$	$[N\times 1]$	Initial sate vector consists of positions, speed and phase starting with correspond frequencies of the rover
$\mathbf{P}_k$	$[N\times N]$	Estimated error covariance matrix
$\mathbf{F}_k^{k+1}$	$[N\times M]$	Matrix of state equation
$\mathbf{w}_k$	$[N\times 1]$	State the noise vector with covariance matrix $\mathbf{Q}_k^{k+1}$
$\mathbf{Q}_k^{k+1}$	$[N\times N]$	Covariance matrix in state estimation
$\mathbf{x}_p$	$[N\times 1]$	Predicted state vector
$\mathbf{P}_p$	$[N\times N]$	Predicted error covariance matrix
$\mathbf{H}(\bullet)$	$[M\times M]$	Measurement equation matrix
$\mathbf{M}_k$	$[M\times M]$	Measurement covariance matrix corresponding to vector $\mathbf{z}_k$
$\mathbf{K}_k$	$[M\times M]$	Kalman filter gain matrix
$\mathbf{z}_k$	$[M\times 1]$	Measured value vector
$\mathbf{h}(\mathbf{x}_p)$	$[M\times 1]$	Predicted measurement vector
$\mathbf{I}$	$[M\times M]$	Identity matrix
$\hat{\mathbf{x}}_{k+1}$	$[N\times 1]$	Estimated state vector corresponds to $\hat{\mathbf{x}}_k$
$\mathbf{P}_{k+1}$	$[N\times N]$	Re-estimated covariance matrix

From Table 2.1, state vector can be expressed as

$$\mathbf{x}_k = (\mathbf{r}_r^T, \mathbf{v}_r^T, \mathbf{N}_{i,rb}^T)_k^T, \tag{2.25}$$

where $\mathbf{r}_r$ is the rover position in ECEF-coordinates (*x, y, z*) and vector $\mathbf{r}_r$ is the speed of rover in m/s which can be expressed as

$$\mathbf{v}_r = (v_e, v_n, v_u), \tag{2.26}$$

and $\mathbf{N}_{i,rb}$ represents the carrier-phase ambiguity as

$$\mathbf{N}_{i,rb} = (N_{i,rb}^1, N_{i,rb}^2, ..., N_{i,rb}^m)^T, \tag{2.27}$$

where i is the frequency such as L1, L2 or L5. For measured value vector $\mathbf{z}_k$, it can be defined as

$$\mathbf{z}_k = (\mathbf{\Phi}_{rb}^T, \mathbf{P}_{rb}^T)_k^T , \quad 2.28$$

where measured value for carrier-phase consists of

$$\mathbf{\Phi}_{rb}^T = (\phi_{rb}^{12}, \phi_{rb}^{13}, ..., \phi_{rb}^{1m})^T , \quad 2.29$$

and code psudorange is

$$\mathbf{P}_{rb}^T = (\rho_{rb}^{12}, \rho_{rb}^{13}, ..., \rho_{rb}^{1m})^T , \quad 2.30$$

To estimate the state vector, $\hat{\mathbf{x}}_k$ can be divided into following 2 parts.

2.2.3.1 Estimation of the rover position and speed

The matrix $\mathbf{F}_k^{k+1}$ used to estimate the rover position and speed can be express as

$$\mathbf{F}_k^{k+1} = \begin{bmatrix} \mathbf{I}_{3x3} & \tau_r \mathbf{I}_{3x3} & 0 \\ 0 & \mathbf{I}_{3x3} & 0 \\ 0 & 0 & \mathbf{I}_{(3m-3)\times 3m-3)} \end{bmatrix}, \quad 2.31$$

where τ_r the GNSS data sampling period in seconds. The estimation of covariance matrix can be expressed as

$$\mathbf{Q}_k^{k+1} = \begin{bmatrix} \mathbf{0}_{3x3} & 0 & 0 \\ 0 & \mathbf{Q}_v & 0 \\ 0 & 0 & \mathbf{0}_{(3m-3)\times 3m-3)} \end{bmatrix}, \quad 2.32$$

where the matrix $\mathbf{Q}_v$ can be expressed as

$$\mathbf{Q}_v = \mathbf{E}_r^T \, \mathrm{diag}([\tau_r \sigma_{ve}^2 \quad \tau_r \sigma_{vn}^2 \quad \tau_r \sigma_{vu}^2])\mathbf{E}_r , \quad 2.33$$

where σ_{ve}^2 , σ_{vn}^2 and σ_{vu}^2 is the velocity variation along the direction of east, north and vertical, axis, respectively. The $\mathbf{E}_r$ matrix represents the rotation from the reference frame ECEF-coordinate to local coordinates which can be described as

$$\mathbf{E}_r = \begin{bmatrix} -\sin(\lambda_r) & \cos(\lambda_r) & 0 \\ -\sin(\phi_r)\cos(\lambda_r) & -\sin(\phi_r)\sin(\lambda_r) & \cos(\phi_r) \\ \cos(\phi_r)\cos(\lambda_r) & \cos(\phi_r)\sin(\lambda_r) & \sin(\phi_r) \end{bmatrix}, \quad 2.34$$

where (ϕ_r, λ_r) is the rover position in the geodetic coordinates system. The measurement equation matrix $\mathbf{H}(\bullet)$ for frequencies of L1, L2 and L5 can be shown as

$$\mathbf{H}(\bullet) = \begin{bmatrix} -\mathbf{DE} & \mathbf{0} & \lambda_{L1}\mathbf{D} & \mathbf{0} & \mathbf{0} \\ -\mathbf{DE} & \mathbf{0} & \mathbf{0} & \lambda_{L2}\mathbf{D} & \mathbf{0} \\ -\mathbf{DE} & \mathbf{0} & \mathbf{0} & \mathbf{0} & \lambda_{L5}\mathbf{D} \\ -\mathbf{DE} & \mathbf{0} & \mathbf{0} & \mathbf{0} & \mathbf{0} \\ -\mathbf{DE} & \mathbf{0} & \mathbf{0} & \mathbf{0} & \mathbf{0} \\ -\mathbf{DE} & \mathbf{0} & \mathbf{0} & \mathbf{0} & \mathbf{0} \end{bmatrix}, \quad 2.35$$

where $\mathbf{D}$ is the transformation matrix from SD to DD can be written as

$$\mathbf{D} = \begin{bmatrix} 1 & -1 & 0 & \cdots & 0 \\ 1 & 0 & -1 & \cdots & 0 \\ \vdots & \vdots & \vdots & \ddots & \vdots \\ 1 & 0 & 0 & \cdots & -1 \end{bmatrix}. \quad 2.36$$

Given that $\mathbf{E}$ be the set of the vectors in the line of sight from the rover to the satellite in ECEF-coordinates, i.e.,

$$\mathbf{E} = (e_r^1, e_r^2, ..., e_r^m)^T, \quad 2.37$$

where e_r^1 is vector on ECEF coordinate system with the direction from rover's line of sight to the satellite 1. Then, the measurement covariance matrix is used to estimate the rover position and velocity as follows:

$$\mathbf{M}_k = \begin{bmatrix} \mathbf{D}\mathbf{M}_{\phi_{L1}}\mathbf{D}^T & 0 & 0 & 0 & 0 & 0 \\ 0 & \mathbf{D}\mathbf{M}_{\phi_{L2}}\mathbf{D}^T & 0 & 0 & 0 & 0 \\ 0 & 0 & \mathbf{D}\mathbf{M}_{\phi_{L5}}\mathbf{D}^T & 0 & 0 & 0 \\ 0 & 0 & 0 & \mathbf{D}\mathbf{M}_{\rho_{L1}}\mathbf{D}^T & 0 & 0 \\ 0 & 0 & 0 & 0 & \mathbf{D}\mathbf{M}_{\rho_{L2}}\mathbf{D}^T & 0 \\ 0 & 0 & 0 & 0 & 0 & \mathbf{D}\mathbf{M}_{\rho_{L5}}\mathbf{D}^T \end{bmatrix}, \quad 2.38$$

where $\mathbf{M}_{\phi_i}$ is the covariance matrix in the carrier-phase measurement at frequency i between receivers of GNSS signals to each satellite which can be written as

$$\mathbf{M}_{\phi_i} = \mathrm{diag}\left(\left[2(\sigma_{\phi_i}^1)^2, 2(\sigma_{\phi_i}^2)^2, ..., 2(\sigma_{\phi_i}^m)^2\right]\right). \quad 2.39$$

Similarly, covariance matrix of the code psudorange measurement $\mathbf{R}_{\rho_i}$ can be written as

$$\mathbf{M}_{\rho_i} = \mathrm{diag}\left(\left[2(\sigma_{\rho_i}^1)^2, 2(\sigma_{\rho_i}^2)^2, ..., 2(\sigma_{\rho_i}^m)^2\right]\right). \quad 2.40$$

The prediction measurement vector $\mathbf{h}(\mathbf{x}_p)$ can be written as

$$\mathbf{h}(\mathbf{x}_p) = (\mathbf{h}_{\phi_{L1}}^T, \mathbf{h}_{\phi_{L2}}^T, \mathbf{h}_{\phi_{L5}}^T, \mathbf{h}_{\rho_{L1}}^T, \mathbf{h}_{\rho_{L2}}^T, \mathbf{h}_{\rho_{L5}}^T)^T, \quad 2.41$$

where carrier-phase measurement matrix $\mathbf{h}_{\phi_i}$ can be written as

$$\mathbf{h}_{\phi_i} = \begin{bmatrix} \rho_{rb}^{12} + \lambda_i(N_{i,rb}^1 - N_{i,rb}^2) \\ \rho_{rb}^{13} + \lambda_i(N_{i,rb}^1 - N_{i,rb}^3) \\ \vdots \\ \rho_{rb}^{1m} + \lambda_i(N_{i,rb}^1 - N_{i,rb}^m) \end{bmatrix}^T. \quad 2.42$$

Similarly, the code psudorange measurement matrix $\mathbf{h}_{\rho_i}$ can be written as

$$\mathbf{h}_{\rho_i} = \begin{bmatrix} \rho_{rb}^{12} \\ \rho_{rb}^{13} \\ \vdots \\ \rho_{rb}^{1m} \end{bmatrix}^T. \quad 2.43$$

Then, we will discuss the estimation of the integer ambiguity resolution with the Least-Squares Ambiguity Decorrelation (LAMBDA) in the following section.

2.2.3.2 Integer ambiguity resolution using LAMBDA

The procedure for integer ambiguity resolution is shown in Figure 2.16.

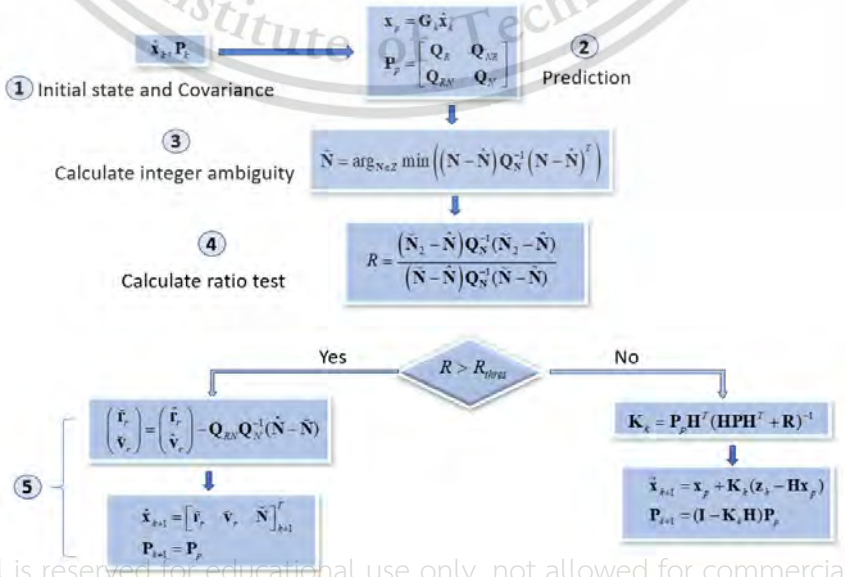

Figure 2.16 Steps for integer ambiguity resolution

The state and measurement equations are represented by

$$\mathbf{G} = \begin{bmatrix} \mathbf{I}_{6\times6} & 0 & 0 & 0 \\ 0 & \mathbf{D} & 0 & 0 \\ 0 & 0 & \mathbf{D} & 0 \\ 0 & 0 & 0 & \mathbf{D} \end{bmatrix}. \quad 2.44$$

After calculating $\mathbf{x}_p$ and $\mathbf{P}_p$ with the matrix $\mathbf{G}$, the matrix $\mathbf{Q}_N$ is used to estimate the integer ambiguity using integer lease square (ILS) problem as

$$\breve{\mathbf{N}} = \arg_{\mathbf{N}\in Z} \min\left(\left(\mathbf{N}-\hat{\mathbf{N}}\right)\mathbf{Q}_{\mathbf{N}}^{-1}\left(\mathbf{N}-\hat{\mathbf{N}}\right)^{T}\right). \quad 2.45$$

To solve the ILS problem, the LAMBDA method is applied. The LAMBDA method offers the combination of a linear transformation to shrink integer vector search space and a skillful tree-search procedure in the transformed space. The integer vector solution by these procedures is validated by the following simple "ratio test". In the "ratio test," the ratio-factor γ, defined as the ratio of the weighted sum of the squared residuals by the second-best solution $\breve{\mathbf{N}}_2$ to one by the $\breve{\mathbf{N}}_1$, is used to check the reliability of the solution. The validation threshold γ_{thres} can be defined from

$$\gamma = \frac{\left(\breve{\mathbf{N}}_2-\hat{\mathbf{N}}\right)\mathbf{Q}_{\mathbf{N}}^{-1}(\breve{\mathbf{N}}_2-\hat{\mathbf{N}})}{\left(\breve{\mathbf{N}}-\hat{\mathbf{N}}\right)\mathbf{Q}_{\mathbf{N}}^{-1}(\breve{\mathbf{N}}-\hat{\mathbf{N}})} > \gamma_{thres}. \quad 2.46$$

After validation, the "fixed" solution of the rover position $\breve{\mathbf{r}}_r$ and velocity $\breve{\mathbf{v}}_r$ are obtained by solving the following equation. If the validation fails, "RTKLIB" outputs the "float" solution of $\hat{\mathbf{r}}_r$ and $\hat{\mathbf{v}}_r$. The availability of "fixed" and float solution can vary on the value of threshold. Practically, the fix solutions which exceed the ratio of 2 can be reliable.

2.2.4 Evaluation parameters for RTK positioning performance

To evaluate the positioning performance, horizontal positioning error (HPE) and vertical positioning error (VPE) are typically computed. For example, VPE can simply be computed from the difference of heights between RTK position and true position, i.e.,

$$VPE = h_{RTK} - h_{True}, \quad 2.47$$

where h_{RTK} and h_{True} are the height from RTK position and actual high correspondingly. Similarly, HPE can be computed with Haversine formula [47] from the difference of latitudes

between RTK positioning and True Position (Δlat) and longitudinal difference between RTK positioning and true positioning (Δlon), i.e.,

$$a = \sin^2(\frac{\Delta lat}{2}) + \cos(lat_{RTK})\cos(lat_{True}).\sin^2(\frac{\Delta lon}{2}), \quad 2.48$$

$$\upsilon = a.\text{atan2}(\sqrt{a}, \sqrt{1-a}), \quad 2.49$$

$$\text{atan2}(\sqrt{a}, \sqrt{1-a}) = \begin{cases} \arctan(\frac{\sqrt{a}}{\sqrt{1-a}}) & \text{if } \sqrt{1-a} > 0 \\ \arctan(\frac{\sqrt{a}}{\sqrt{1-a}}) + \pi & \text{if } \sqrt{1-a} < 0 \text{ and } \sqrt{a} \geq 0 \\ \arctan(\frac{\sqrt{a}}{\sqrt{1-a}}) - \pi & \text{if } \sqrt{1-a} < 0 \text{ and } \sqrt{a} < 0 \\ +\frac{\pi}{2} & \text{if } \sqrt{1-a} = 0 \text{ and } \sqrt{a} > 0 \\ -\frac{\pi}{2} & \text{if } \sqrt{1-a} = 0 \text{ and } \sqrt{a} < 0 \\ \text{undefined} & \text{if } \sqrt{1-a} = 0 \text{ and } \sqrt{a} = 0 \end{cases}, \quad 2.50$$

and

$$HPE = r_{earth}.\upsilon, \quad 2.51$$

where r_{earth} is the radius of Earth (6371 km)

2.3 Ground-based augmentation system (GBAS) and ionospheric delay gradient

We also study the effects of PEBs on ionospheric delay gradients for ground-based augmentation system (GBAS). GBAS is commonly used in the aircraft navigation system, during many phases of a flight. The international Civil Aviation Organization (ICAO) has proposed GBAS [48] as an ICAO standard for auto-landing system in an aircraft, on or after landing phase within 42.6 km (23 nautical miles) from an airport [49]. GBAS provides corrections and integrity information for global navigation satellite system (GNSS) signals to provide navigation guidance for precision approach and landing for civil aviation. GBAS is based on the differential GNSS technique, whereby errors in GNSS range measurements are corrected in the range domain. The corrections delivered in real time are based on measurements by multiple ground reference GNSS receivers usually placed at or near an airport with their locations precisely known. In GBAS, the ionospheric delay is corrected as a part of the total ranging error including tropospheric delay, satellite clock error, and satellite ephemeris error from the range measurements recorded by the reference receivers. These

differential corrections are valid as long as the ionospheric delay is homogeneous in space. Since the ionosphere is spatially variable, however, differential correction errors associated with spatial decorrelation of the ionospheric delay, or in other words ionospheric spatial gradients, must be considered and mitigated [1]. In GBAS, background gradients of ionospheric delays, commonly termed ‘‘nominal ionospheric gradients,’’ are mitigated by determining a conservative one-sigma parameter (σ_{vig}) to bound the uncertainty in the nominal vertical ionospheric delay gradient [48]. However, it is known that ionospheric delay may greatly deviate from nominal levels due to various disturbances [50].

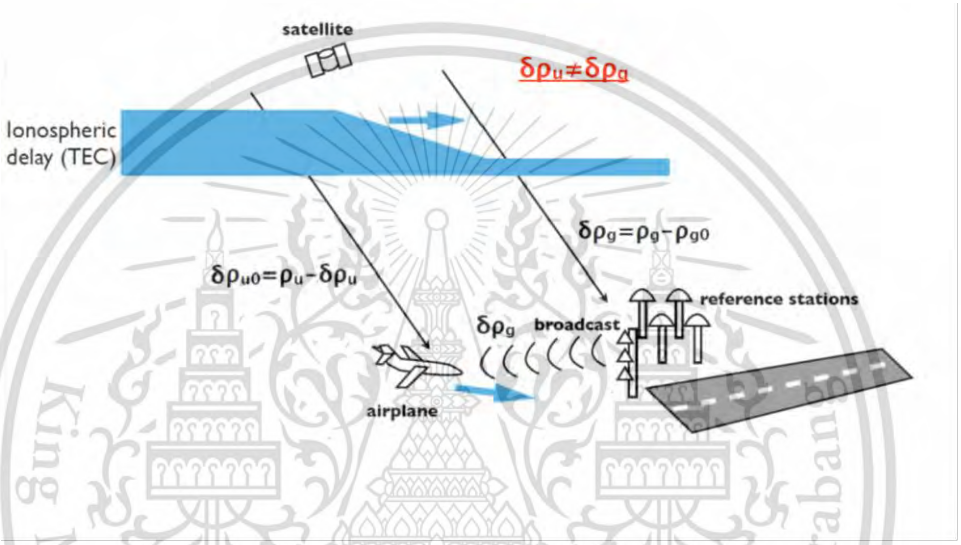

Figure 2.17 Impact of ionospheric gradients on ground-based augmentation system

2.3.1 Ionospheric delay gradient computation

Single frequency carrier-based code aided (SF-CBCA) method was developed by the Electronic Navigation Research Institute, Japan [51]. SF-CBCA uses single-frequency carrier phase and code measurements to estimate ionospheric delay differences between a pair of GNSS receivers [51]. The distance between a GPS receiver and satellites from a single frequency can be measured based on code pseudorange (ρ^p) and carrier phase (Φ^p) [52] as

$$\Phi^p = R^p + b - B^p + T^p + \lambda N^p + \varepsilon_\phi^p , \quad 2.52$$

$$\rho^p = R^p + b - B^p + \delta I^p + \varepsilon_p^p , \quad 2.53$$

where R is the geometic range between a receiver and the satellite (m), the subscrpit p represents the satellite number, b is the receiver clock bias (m), B is satellite clock bias(m), δI is the ionospheric delay (m), T is the tropospheric delay (m), N is the integer ambiguity (cycle), and ε is the measurement noise relative to the multipath effect. The ionospheric-free combination

L is used to remove the ionosphere term, the geometry range and satellite clock bias effect with the single difference (SD) between two stations ("a" and "b"), i.e.,

$$L^P = \frac{\Phi^p + \rho^p}{2} - \gamma^p, \tag{2.54}$$

and

$$L^p_{SD} = L^p_a - L^p_b = b_{SD} - \frac{\lambda}{2} N^p_{SD} + \frac{\varepsilon^p_{\phi,SD} + \varepsilon^p_{p,SD}}{2}. \tag{2.55}$$

The geometry-free carrier phase with single difference can be computed from

$$\Phi^p_{SD} = \Phi^p_a - \Phi^p_b, \tag{2.56}$$

and

$$R^p_{SD} = R^p_a - R^p_b, \tag{2.57}$$

then

$$\phi^p_{SD} = \Phi^p_{SD} - R^p_{SD} = b_{SD} - \delta I^p_{SD} + \lambda N^p_{SD} - \varepsilon^p_{\phi,SD}. \tag{2.58}$$

In equation (19) and (22)The tropospheric delay gradient is assumed to be zero. These two equation can be expressed as the matrix [52] as

$$\begin{bmatrix} \mathbf{\Phi}_{SD} \\ \mathbf{L}_{SD} \end{bmatrix} = \begin{bmatrix} 1 & -\mathbf{I} & \lambda\mathbf{I} \\ 1 & 0 & \lambda\mathbf{I} \end{bmatrix} \begin{bmatrix} b_{SD} \\ \delta\mathbf{I}_{SD} \\ \mathbf{N}_{SD} \end{bmatrix} + \begin{bmatrix} \varepsilon_{\phi,SD} \\ \dfrac{\varepsilon_{\phi,SD} + \varepsilon_{p,SD}}{2} \end{bmatrix}, \tag{2.59}$$

Once the matrix of linear equation is identified, the Kalman filter is used to estimate b_{SD}, $\delta\mathbf{I}_{SD}$, and $\mathbf{N}_{SD}$ to float solution as the number of equations is fewer than the number of unknown parameters. Particularly, the estimated parameters from the Kalman filter still contain decimals and the integer ambiguities $\mathbf{N}_{SD}$ must consist of the integer values only. The least-square ambiguity decorrelation adjustment (LAMBDA) method is applied to fix the float values [53]. To estimate the appropriate integer solution, they are modified to the double difference of integer ambiguities ($\hat{\mathbf{N}}_{DD}$). Afterwards, the LAMBDA method is to provide the best and second best of the integer candidates ($\breve{\mathbf{N}}_{DD,1st}$, $\breve{\mathbf{N}}_{DD,2nd}$) for the validation step. The validation of the integer ambiguities is a key to measure the reliability of integer solution. The ratio test, based on the best and second-best candidates, compares the ratio of the corresponding errors with the success ratio threshold (γ_{thres}), which is,

$$\frac{(\hat{\mathbf{N}}_{DD} - \breve{\mathbf{N}}_{DD,2nd})^T \mathbf{P}^{-1}_{\hat{\mathbf{N}}_{DD}} (\hat{\mathbf{N}}_{DD} - \breve{\mathbf{N}}_{DD,2nd})}{(\hat{\mathbf{N}}_{DD} - \breve{\mathbf{N}}_{DD,1st})^T \mathbf{P}^{-1}_{\hat{\mathbf{N}}_{DD}} (\hat{\mathbf{N}}_{DD} - \breve{\mathbf{N}}_{DD,1st})} > \gamma_{thres}, \tag{2.60}$$

where $\mathbf{P}_{\hat{\mathbf{N}}_{DD}}$ is the covariance matrix of double difference inter ambiguities and ratio thresholds (R) is typically set to 2 or 3. The higher the value of R, the stronger the reliability is. When successful solutions of integer ambiguities in the double difference form ($\hat{\mathbf{N}}_{DD}$) are obtained, they are used to adjust the SD of the ionospheric delay ($\boldsymbol{\delta}\hat{\mathbf{I}}_{SD}$) to the fixed solution ($\boldsymbol{\delta}\breve{\mathbf{I}}_{SD}$) from

$$\boldsymbol{\delta}\breve{\mathbf{I}}_{SD} = \boldsymbol{\delta}\hat{\mathbf{I}}_{SD} - \mathbf{P}_{\hat{N}}\mathbf{P}_{\hat{N}}^{-1}(\hat{\mathbf{N}}_{DD} - \breve{\mathbf{N}}_{DD}) . \quad 2.61$$

Furthermore, by using three GNSS receivers, which give three unique combinations of two GNSS receivers, the validity of the solutions can be checked by taking the cyclic sum of the ionospheric delay differences from the three pairs[18] as followed,, i.e.,

$$\delta I^{p}_{SD,i,j} = \delta I^{p}_{i} - \delta^{p}_{j} , \quad 2.62$$

$$I^{p}_{SD,i,j} = \delta I^{p}_{i} - \delta I^{p}_{j} , \quad 2.63$$

$$I^{p}_{SD,j,k} = \delta I^{p}_{j} - \delta I^{p}_{k} , \quad 2.64$$

$$I^{p}_{SD,k,i} = \delta I^{p}_{k} - \delta I^{p}_{i} . \quad 2.65$$

If the solution is solved consistently,

$$I^{p}_{SD,i,j} + I^{p}_{SD,j,k} + I^{p}_{SD,k,i} \approx 0 . \quad 2.66$$

Only the solutions that pass this consistency check are considered reliable. During this study, we use 0.2 as threshold.

The next step is to compute the ionospheric delay gradients as shown in Figure 2.18. The SD term is converted into the ionospheric gradient term $\Delta\mathbf{I}$ (mm/km) [55] from

$$\Delta\mathbf{I} = \frac{\boldsymbol{\delta}\breve{\mathbf{I}}_{SD}}{d} , \quad 2.67$$

where d is the baseline between the two receivers (km). The baseline should not encounter the tropospheric delay gradients or nonlinear effects in the ionosphere [56], which is typically more than about 50 km.

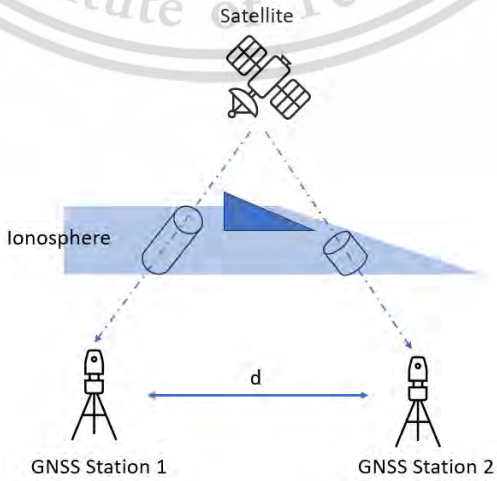

Figure 2.18 Ionospheric delay gradients between two GNSS stations

2.4 Machine learning in ionospheric anomaly detection

Machine learning models are widely applied in various research areas including medical terminology, business, automation, language recognition, finance and various forecasting applications. There are different types of machine learning models such as artificial neural network (ANN), recurrent neural network (RNN), long short-term memory network (LSTM), support vector machine (SVM), convolutional neural network (CNN) and so on. Utilize the machine learning model also increasing in space weather applications such as TEC prediction, foF2 prediction, ionospheric disturbance prediction and so on [23], [25], [42], [57]–[59]. Therefore, as an addition to our work, we also apply machine learning algorithms in ionospheric disturbance prediction applications. We use a conventional long short-term memory (LSTM) model with a next frame prediction approach for predicting the EPBs using ionospheric ROTI maps.

2.4.1 Convolutional long short-term memory (LSTM) model

A convolutional LSTM (Long Short-Term Memory) model is a neural network architecture that combines the strengths of both convolutional neural networks (CNNs) and LSTMs. CNNs are primarily used for image recognition and computer vision tasks due to their ability to adaptively learn spatial hierarchies of features from input images. LSTMs are type of recurrent neural network (RNN) designed to handle sequential data allowing them to capture dependencies in data over extended period of time. By combining the CNN and LSTM, convolutional LSTMs incorporate convolutional operations within LSTM architecture, allowing them to capture spatial features as well as temporal dependencies. It is particularly well-suited for tasks involving spatiotemporal data, such as video analysis, weather forecasting, and other spatial temporal dependencies [60]. The mathematical model for a Convolutional LSTM (Long Short-Term Memory) combines the equations of both CNNs (Convolutional Neural Networks) and LSTMs (Long Short-Term Memory) to capture spatial-temporal patterns in sequential data [61]. An example of the generic convolutional LSTM is shown in Figure 2.19.

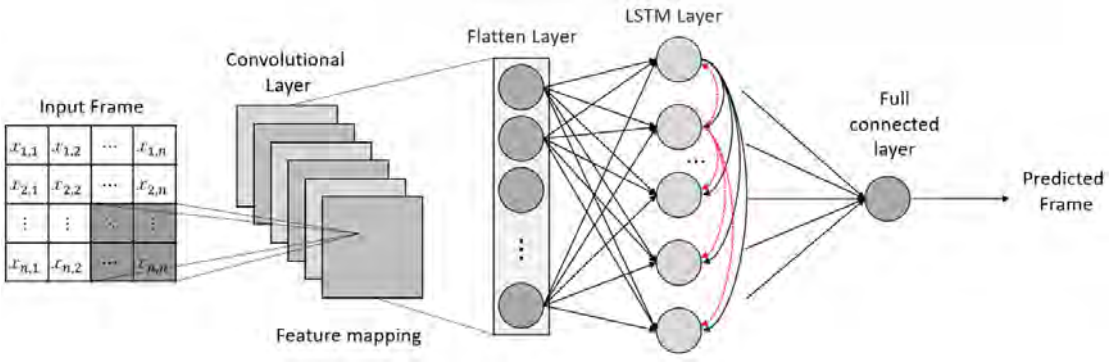

Figure 2.19 General structure of the convolutional LSTM model

The mathematical model of convolution LSTM model includes 4 parts: convolutional layers, LSTM layers, Temporal Modeling and Output layer [62]. The convolutional layers in a Convolutional LSTM model perform convolution operations on the input data to extract spatial features. Each convolutional layer is presented mathematically as

$$H^i = f(W^i \times X + b^i), \quad 2.68$$

where H^i represents the feature map or activation map after the i^{th} convolutional layer, W^i denotes the convolutional filter or kernel for the i^{th} layer, X is the input data, b^i is the bias term and *f* is the activation function. We use "sigmoid" activation function in our study.

The LSTM layers process the output of the convolutional layers while capturing temporal dependencies. The LSTM cell consists of several equations. Input gate (i), forget gate (f), and output gate (o) can be express as

$$i_t = \sigma(W_{ix}.X_t + W_{ih}.H_{t-1} + b_i), \quad 2.69$$

$$f_t = \sigma(W_{fx}.X_t + W_{fh}.H_{t-1} + b_f), \quad 2.70$$

$$o_t = \sigma(W_{ox}.X_t + W_{oh}.H_{t-1} + b_o), \quad 2.71$$

where i_t, f_t and o_t ae the input, forget and output gates at time *t*, respectively. X_t is the input at time *t* and H_{t-1} is the hidden state of LSTM cell at time *t-1*, *W* is the bias weight matrix and *b* is the bias terms. σ represents the sigmoid activation function.

The cell sate update (c_t) performs as

$$g_t = \tanh(W_{gx}.X_t + W_{gh}.H_{t-1} + b_g), \quad 2.72$$

$$c_t = f_t.c_{t-1} + i_t.g_t, \quad 2.73$$

where g_t is the candidate cell state and c_t is the updated cell state at time *t*.

Hidden state (H_t) can be expressed as

$$H_t = o_t.\tanh(c_t), \quad 2.74$$

The LSTM layers process the sequence of spatial features (H_t) across time (*t*) to capture temporal patterns and dependencies.

The output from the LSTM layers can be used for various tasks, such as classification, regression, or sequence generation, depending on the specific application.

2.4.2 Sigmoid activation function

Activation functions are mainly used to originate non-linear variations in the neural networks. In this work, we use sigmoid activation function and sigmoid function has good properties as an activation function. The main reason why we use sigmoid function is because it exists between 0

and 1. Therefore, it is very efficient for model to predict the probability as an output since probability of anything exists only between the range of 0 and 1, sigmoid is the right choice. Sigmoid function can be expressed as [63],

$$\sigma(x) = \frac{1}{1+e^{-x}}. \tag{2.75}$$

The output of the function is shown in Figure 2.20.

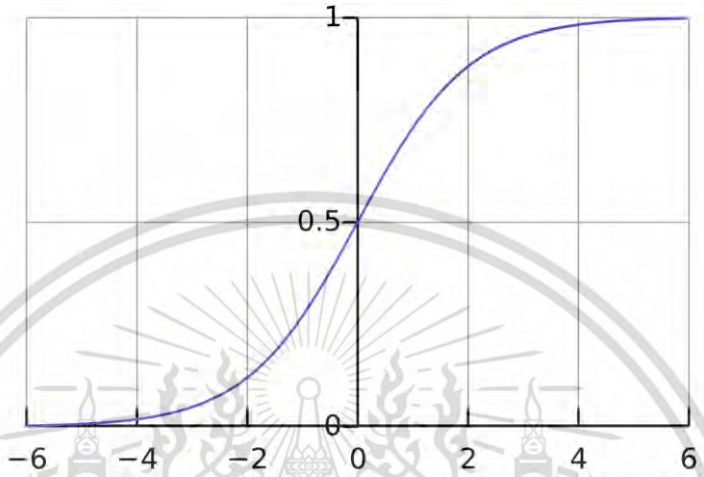

Figure 2.20 Sigmoid activation function

2.4.3 Evaluation parameters for machine learning prediction

To evaluate the performance of machine learning model, we will use mean squared error (MSE) and structural similarity index (SSIM) by comparing the two images. MSE between image can be computed as

$$MSE = \frac{1}{mn}\sum_{i=0}^{m-1}\sum_{j=0}^{n-1}\left\| f(i,j) - g(i,j)\right\|^2, \tag{2.76}$$

where f represents the matrix data of actual image, g represents the matrix data of predicted images, m represents the numbers of pixels of the image and i represents the index of that row, n represents the number of columns of the image and j represents the index of that column.

SSIM is a quality assessment index based on the computation of three factors: luminance(l), contrast(c) and structure (s). SSIM can be express as

$$SSIM(x,y) = \left[l(x,y)\right]^{\alpha} \times \left[c(x,y)\right]^{\beta} \times \left[c(x,y)\right]^{\gamma}, \tag{2.77}$$

where

$$l(x,y) = \frac{2\mu_x\mu_y + C_1}{\mu_x^{\,2} + \mu_y^{\,2} + C_1}, \tag{2.78}$$

$$c(x,y) = \frac{2\sigma_x\sigma_y + C_2}{\sigma_x^{\,2} + \sigma_y^{\,2} + C_2}, \tag{2.79}$$

$$s(x,y)=\frac{\sigma_x y+C_3}{\sigma_x\sigma_y+C_3}, \quad 2.80$$

where μ_x, μ_y, σ_x, σ_y are the local means, standard deviations, and cross-covariance for image x, y. If we assume $\alpha=\beta=\gamma=1$ and $C_3=C_2/2$, SSIM can simply computed as

$$SSIM(x,y)=\frac{(2\mu_x\mu_y+C_1)(\sigma_x y+C_2)}{({\mu_x}^2+{\mu_y}^2+C_1)({\sigma_x}^2+{\sigma_y}^2+C_2)}. \quad 2.81$$

The SSIM values range between 0 to 1 where 1 means a perfect match the actual image and predicted image.

2.5 Previous works related to the research in this thesis

A number of previous works have studied the ionosphere effects on GNSS precise positioning system as well as aeronautical navigation systems such as ground-based augmentation system (GBAS) and as summarized in Table 2.2. The majority of the previous studies related to precise positioning performance are focused on global ionospheric disturbance at mid and high latitude. Some previous works also explored the use of machine learning in ionospheric studies, as summarized in Table 2.3. However, there is still little work in low-latitude regions. This thesis aims to spotlight the impact of low-latitude ionospheric disturbances, particularly those related to EPBs, on positioning and navigation systems in low-latitude regions. Additionally, we propose employing a machine learning technique for predicting disturbances in the ionosphere specific to low-latitude areas.

Table 2.2 Summary of previous works related to ionospheric disturbance effect or positioning and navigation system

Previous works	Summary of works
[14] Paziewski Jacek et al, *Journal of Space Weather and Space Climate*, 2022	Observed grading accuracy during storm disturbed duration RTK positioning in Greenland during 2015 St. Patrick's Day Strom and
[15] Yang et al., *Journal of Geophysical Research: Space Physics,* 2020	Observed PPP accuracy degradation of up 10 m in high latitudes and 2 m in low-latitudes during 2015 St. Patrick's Day Storm
[17] Zakharenkova et al., *GPS Solutions,* 2021	Presented the meter-level degradation of precise positioning accuracy in the American sector multi-site GNSS network caused by EPB
[3] Jacobsen et al., *Journal of Space Weather and Space Climate,* 2014	Highlighted the statistical strong correlation between ionospheric disturbance and GNSS positioning in high latitude during 2012

[20] Li et al., *Space Weather*, 2022	Observed the meter-level accuracy of kinematic PPP at disturbed time especially during geo storms in China region
[18] Guo et al., *ION Pacific PNT,* 2019	Highlighted the occurrence of PPP accuracy degradation during high scintillation intensity in Hong Kong during solar maximum of 2014
[1] Saito et al., *GPS Solution,* 2017	Presented the ionospheric delay gradient model for GBAS in Asia Pacific Region
[55] Budtho et al., *Radio Science*, 2018	Studied the quiet time ionospheric delay gradients near Suvarnabhumi airport

Table 2.3 Summary of previous works related to utilization of machine learning in previous studies

Previous works	**Summary of works**
[23] Shi et al., *Space Weather,* 2022	Proposed bidirectional LSTM model to create TEC prediction maps over China region
[24] Reddy et al., *Journal of Geophysical Research: Space Physics,* 2023	Proposed a machine learning approach using random forest aggressor for EPB prediction using the SWARM satellite data
[25] Liu et al., *Geophysical Research Letters*, 2021	Proposed machine learning based prediction of ionospheric disturbance using ROTI maps in mid and high-latitude regions
[64] Thammavongsy et al., *Earth, Planets and Space,* 2023	Proposed Spread-F prediction model for Thailand region using LSTM model with ionosonde data
[65] Weng el al., *Remote Sensing,* 2023	Proposed TEC prediction model based on the combination of IRI model and statical machine learning model

Chapter 3 The designed and proposed methods

In this chapter, we will discuss the proposed experimental studies on the effects of ionospheric disturbance over RTK positioning and ionospheric delay gradients for GBAS. We will also discuss proposed study for utilization of machine learning model in ionospheric disturbance prediction.

3.1 Experimental study on the effects of EPBs over RTK positioning system in Thailand

In this work, we propose an experimental study for analyzing the effects of ionospheric disturbances on the RTK positioning at different baseline distances between the base and rover station near the Suvarnabhumi International Airport, Bangkok Thailand. We focus on the GPS constellation only. As shown in Figure 3.1, KMIG station is used as the base station. Three rover stations, AER1, STFD and DPT9 stations are used for the short (4 km), medium (12 km) and long (21 km) baselines from the base station, respectively. The locations of all GNSS stations existing in our research network since 2010 are described in Table 3.2. All GNSS stations used in this study are equipped with geodetic grade antennas and receivers. All receivers are located in open-sky environments without noticeable multi-path issues.

Figure 3.1 Locations of GNSS stations in Bangkok used in this study

The GPS observation data are in 2020 (solar minimum) and 2022 (ascending phase toward solar maximum), respectively. The RTK positioning errors are processed during quiet periods (daytime) and disturbed periods (nighttime) at different baseline distances on disturbed days (as indicated by ROTI). We use both the RINEX2 observation data to analyze GPS-only positioning errors. For the global geomagnetic activity, the geomagnetic activity (Kp) information is acquired from a website

called “SpaceWeatherLive” by Parsec vzw, a non-profit organization in Belgium [40] which is based on Kp-index from GFZ Potsdam German Research Center for Geosciences [66]. We use the RTKLIB software to perform post-process RTK positioning. RTKLIB is a free open-source package containing applications designed for real-time navigation and post-process positioning. RTKLIB uses several modes such as Single, PPP and carrier-phase based. RTKLIB parameters used in this study are as shown in Table 3.1.

The elevation angle mask of 15° is set to avoid multi-path errors. The positioning performances are measured using HPE, VPE and the 95-percent errors. The quiet period is selected to be during the daytime from 00:00:00 to 12:00:00 UTC (7:00 AM to 7:00 PM LT), whereas the disturbed period is during nighttime from 12:00:00 to 24:00:00 UTC (7:00 PM to 7:00 AM LT) on the disturbed days. HPE and VPE are computed from the output of RTKLIB according to equation 2.47 - 2.51.

Table 3.1 Parameters for RTKPOST of RTKLIB software used in this Study

Positioning Mode	**Kinematic**
Frequency	L1
Filter Type	Forward
Elevation Mask	15°
Constellation	GPS
Integer Ambiguity Resolution	Continuous
Ratio to fix Ambiguity	3
Antenna Type	*: Auto (Auto phase center adjustment from RINEX obs header)

Additionally, we perform RTK positioning at different latitudes in order to evaluate the positioning errors caused by EPBs over Thailand Region. Figure 3.2 shows the locations of three station pairs at different latitudes to evaluate the positioning performance during disturbed period. The names of the stations with coordinates used in this study are shown in Table 3.2. The summarized simulation and processing procedure to analyze the RTK positioning performance in this study is shown in Figure 3.3.

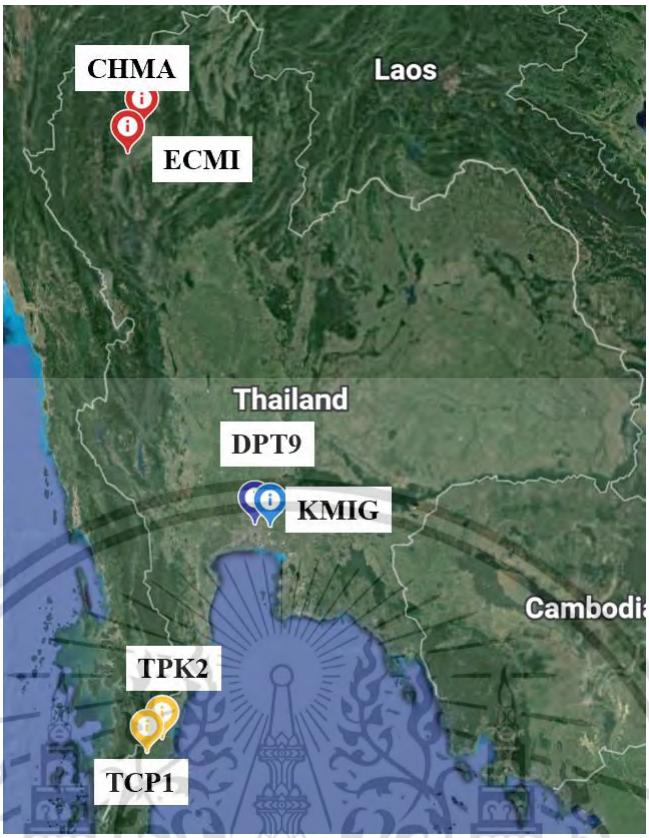

Figure 3.2 GNSS station pairs used to study RTK at different latitudes

Table 3.2 Names and coordinates of GNSS Stations used in this study

Station Names	Geodetic Coordinates			Receivers	Antennas
	Latitude (deg)	Longitude (deg)	Height (m)		
AER1	13.69452 ° N	100.76082 °E	-23.6	Novatel ProPak6	Novatel GPS-703-GGG
DPT9	13.75678 ° N	100.5732 °E	38	LEICA GR50	LEIAR20 LEIM
KMIG	13.72778 ° N	100.77263 °E	25.4	Novatel ProPak7	Novatel GNSS-850
STFD	13.7356 ° N	100.66111 °E	3.7	Novatel ProPak6	Novatel GPS-703-GGG
CHMA	18.83527 ° N	98.96996 °E	296	LEICA GR50	LEIAR20 LEIM
ECMI	18.47368 ° N	98.7891 °E	262.8	LEICA GR50	LEIAR20 LEIM
TCP1	10.80289 ° N	99.17023 °E	31.9	LEICA GR50	LEIAR20 LEIM
TPK2	10.98727 ° N	99.36843 °E	135.9	LEICA GR50	LEIAR20 LEIM

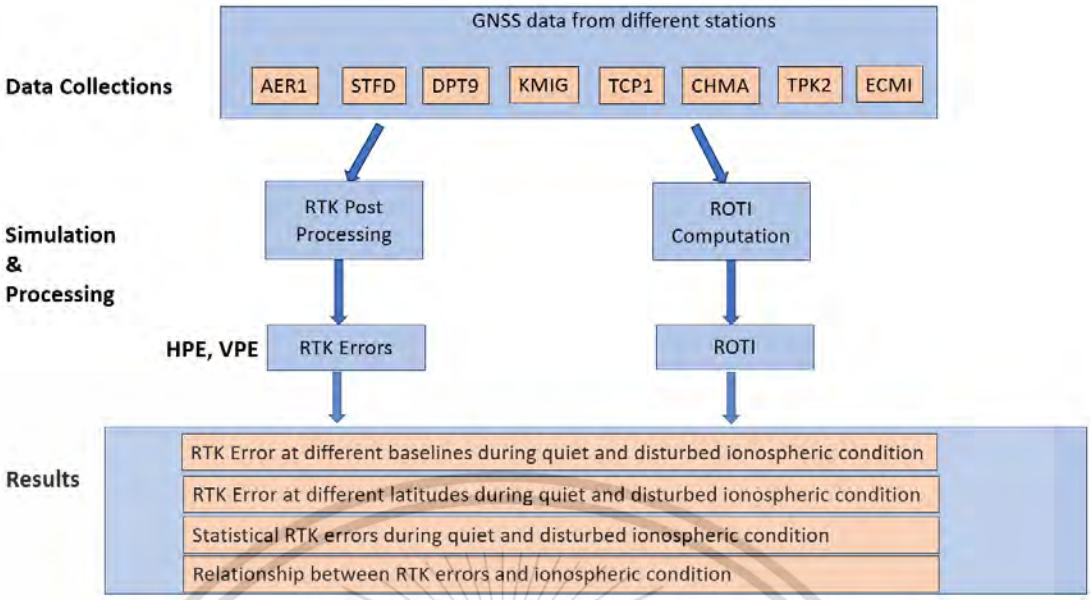

Figure 3.3 Summarized simulation and procedures to analyze RTK positioning performance in this study

3.2 Experimental study on the effects of EPBs on ionospheric delay gradients for GBAS in low-latitude region

In this study, we also propose an experimental study for analyzing the impact of EPBs over ionospheric delay gradients by analyzing the ionospheric delay gradients data near Suvarnabhumi airport over observation data of 2021 from the three GNSS stations pair of KMIT, STFD and AER1. First, we analyze the activity using AATR and after that we analyze and the delay gradients using single-frequency carrier-phase based and code- aided (SF-CBCA) method [51]. Then, we analyze the effect of EPBs on ionospheric delay gradients by comparing the behaviors of ionospheric delay gradients during quiet and disturbed condition. The sources of analyzed observation data are showed in Figure 3.4. The position of GNSS stations is computed relative to each other's as well as with the additional reference stations using AUSPOS - Online GPS Processing Service by Australian Government [67]. Simulation and processing procedures to analyze characteristics of ionospheric delay gradients is in summarized in Figure 3.5.

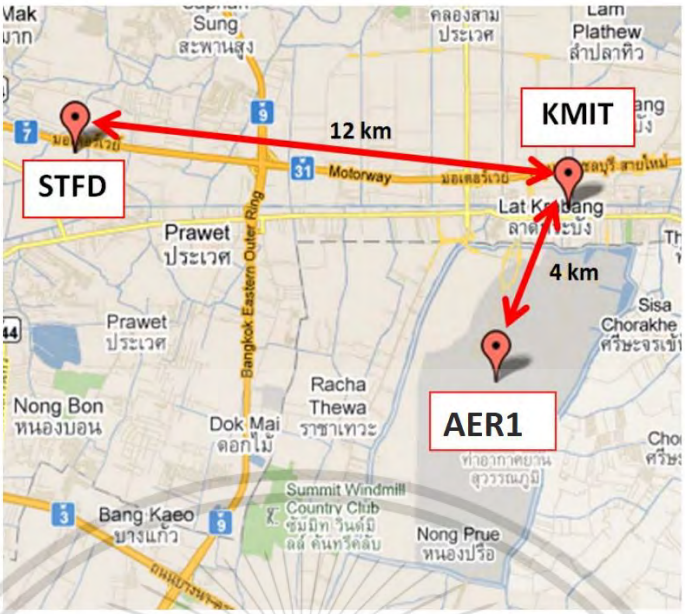

Figure 3.4 Illustrations of the GNSS stations to compute the ionospheric delay gradients near Suvarnabhumi international airport

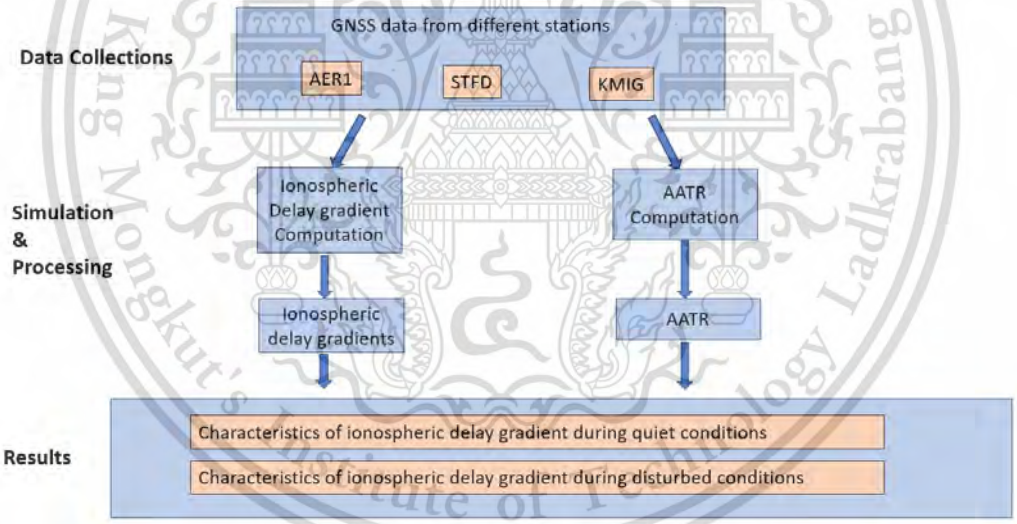

Figure 3.5 Summarized simulation and processing procedures to analyze ionospheric delay gradients in this study

3.3 Development of machine learning models for ionospheric disturbance prediction

In addition, we study the feasibility and applicability of machine learning model in ionospheric disturbance especially for low-latitude ionospheric disturbance prediction such as EPBs. We proposed a machine learning based approach with conventional LSTM to forecast the movement and effected areas of EPBs.

3.3.1 Datasets and data pre-processing

We use existing Thailand regional ROTI maps which are available from the Excellence Center in Thai GNSS and Space Weather Information Data Center. The ROTI Maps are generated from STEC at ionospheric piercing points (IPP), partially at 350 km altitude, based on the observation data of 13 GNSS stations over Thailand regions. The ROTI maps are available with 5-minute temporal resolution video file for each day. Pre-recessing of dataset is performed to be readily used in the convolutional LSTM model. We select the 46 ROTI map video with EPBs from 2022 and each video includes the sequence of 140 frames during night in which EPBs usually occur. Resampling is performed every 25 minutes providing 28 frames for each day. The original frame dimension with 560x420x3 is cropped to 380x340x3 for removing the borders. The cropped frames are resized to half the size of 190x140x3 in order to reduce the training time of the convolutional LSTM model. The final frames are prepared to NumPy array of datasets (samples, timestep(sequence), channel, row, column) to use for training of convolutional LSTM model. Normalization of pixels limit the range to be between 0 and 1. 80 percent of the datasets are used for training and the remaining 20 percent are used for training. The data pre-processing process as shown in Figure 3.6.

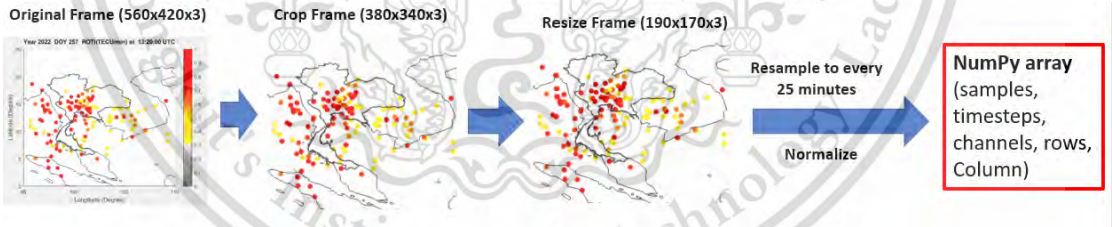

Figure 3.6 Datasets and data pre-processing used for prediction of EPB using convolutional LSTM model

3.3.2 Convolutional LSTM model for EPB prediction

In this study, we proposed a machine learning based approach using convolutional LSTM model with next frame prediction of ROTI map to predict the pattern of ionospheric disturbance. Single convolutional LSTM layer is used and perform experiments with various numbers of filters and LSTM units in order to decide the optimal convolutional LSTM model. The sequence (timesteps) of 5 frames is used for prediction of next frames using the model. The detailed

convolutional LSTM model we used in this study is shown in Figure 3.7 and the parameters of proposed convolutional LSTM model are summarized in Table 3.3. The result of the training the model with various numbers of filters and LSTM cells as well as the prediction performance of the model will be discussed in section 4.3.

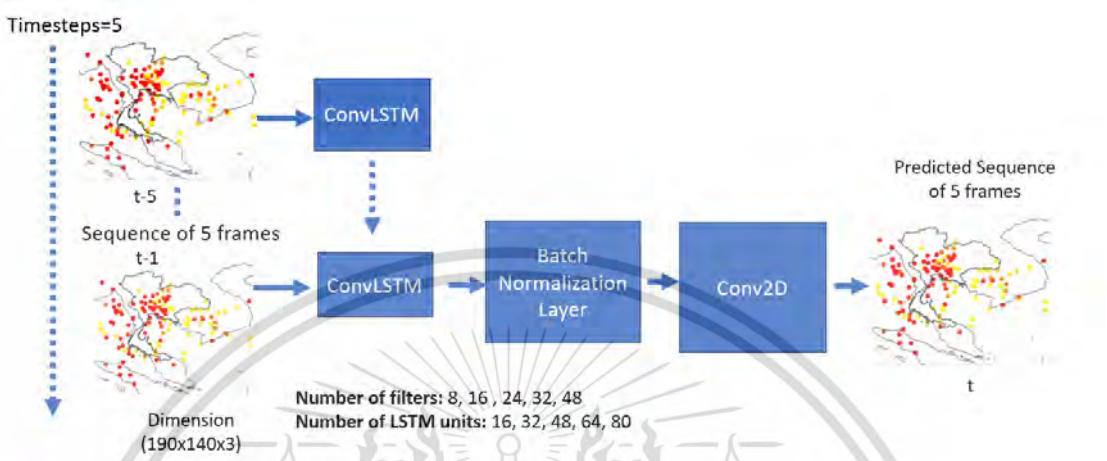

Figure 3.7 Proposed convolutional LSTM model for EPB prediction using ROTI map

Table 3.3 Parameters of proposed convolutional LSTM model for EPB prediction using ROTI Map

Parameter	Value	Description
'input_shape'	190 x 140 x 3	Shape of individual input frame (width, height, channels)
'num_frame_per_sequence'	5	Number of frames in each sequence
'num_filters'	Use various number during training (8, 16, 24, 32, 48)	Numbers of filter used in the ConvLSTM2D layer
'num_lstm_units'	Use various number during training (16, 32, 48, 64, 80)	Number of LSTM units in the ConvLSTM2D layer
'ConvLSTM2D'	(num_filters, (3, 3), 'same', return_sequences=True, input_shape=input_shape)	ConvLSTM2D layer configuration: Number of filters, kernel size, padding ('same'), returning sequences, input shape
'Conv2D'	(3, (3, 3), 'sigmoid', 'same')	Output Conv2D layer: 3 output channels, kernel size, activation

		function ('sigmoid'), padding ('same').
‘model.compile’	optimizer='adam’, loss='mean_squared_error	Compilation of the model using the Adam optimizer and Mean Squared Error (MSE) loss function
‘num_epochs’	100	Number of training epochs

Chapter 4 Results and Discussions

In this chapter, we discuss the results of proposed experimental studies on effects of ionospheric disturbance on RTK positioning and ionospheric delay gradients for GBAS. The performance of convolutional LSTM model and feasibility of machine learning in ionospheric disturbance prediction are also discussed.

4.1 Effects of EPBs on RTK positioning system

In this study, we analyze the impact of ionospheric disturbance on RTK positioning at different baseline lengths as well as in different latitudes. We also present the summary statistics RTK positioning performance during 2020 and 2022. In addition, we also highlight the relationship between ionospheric disturbance (ROTI) and RTK positioning performance.

4.1.1 RTK positioning performances at various baseline lengths during EPB occurrences

We evaluate the RTK positioning performances at different baseline distances at the stations shown in Table 3.2. The computed positioning errors from DOY 314 at 2022 are shown in Figure 4.1 to Figure 4.3 for short, medium, and long baselines, respectively. The X-axis in all rows represent time in UTC which is 7 hours ahead of local time (LT) in Thailand region. The first row represents ROTI from each satellite in different colors. The increase in ROTI, typically larger than 0.8, indicates the occurrence of ionospheric disturbance in Thailand region. The second and third rows indicate the horizontal and vertical positioning errors in which blue color indicates the positioning errors from fix solution and orange color indicates the positioning errors from float solution. The fourth row presents the numbers of usable satellites in RTK positioning system. The percentages of fixed and float solutions are 90.8 and 9.2 percent for short baselines, 68.5 and 31.5 percent for medium baseline, and 46.6 and 53.4 percent for long baseline, respectively. As seen in Figure 4.1 to Figure 4.3, the horizontal and vertical errors of all baseline distances are high during the disturbed periods, and the errors are even higher at longer baseline lengths since the percentage of the fixed solution is lower as shown in Table 4.1. In the case of severe ionospheric disturbances (high ROTI) affecting almost all the satellites, we observe the rapid fluctuation of usable satellite numbers during the disturbed period. According to these results, longer baseline distances correlate with higher error rates, especially during disturbed periods, indicating the challenges in achieving reliable cm-level accuracy under during disturbed periods in low latitudes.

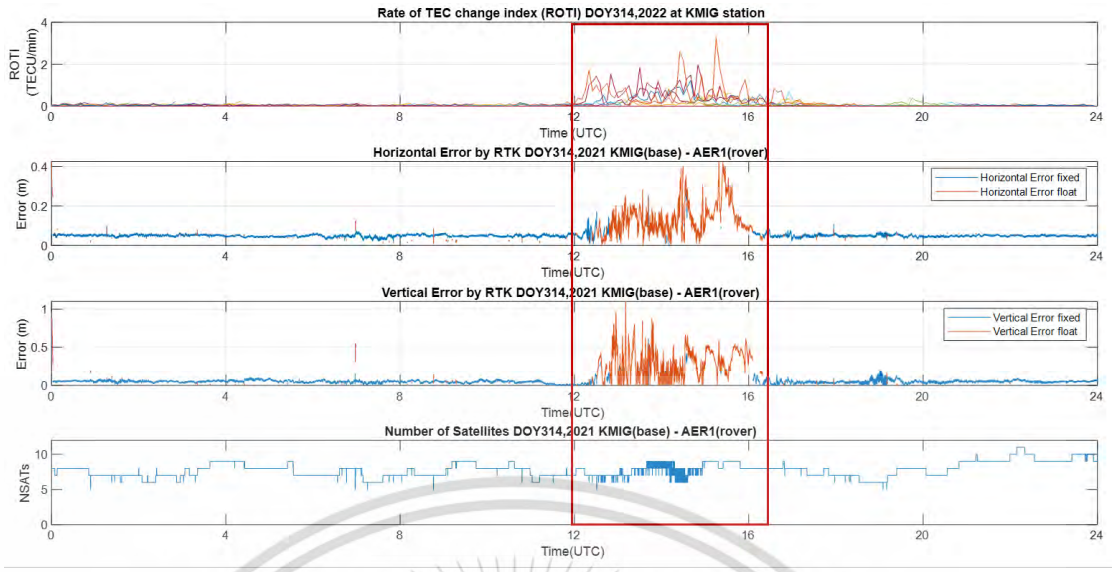

Figure 4.1 Positioning errors on DOY 314, 2022 at a short baseline.

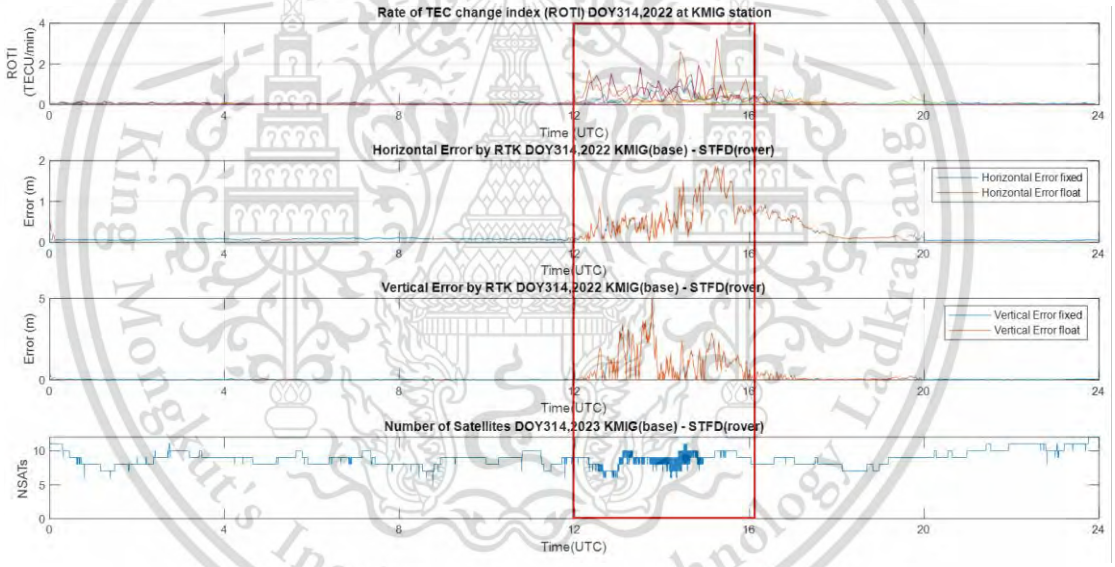

Figure 4.2 Positioning errors on DOY 314, 2022 at a medium baseline.

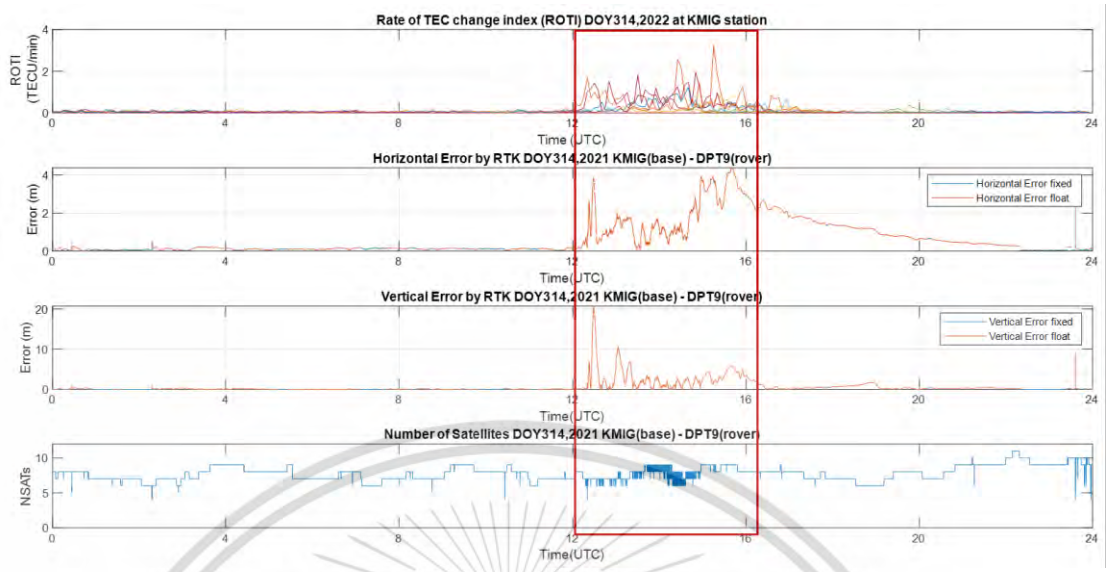

Figure 4.3 Positioning errors on DOY 314, 2022 at a long baseline.

Table 4.1 The 95-percent positioning errors during quiet period(daytime) and disturbed period (nighttime)

Baseline length	Percent of fix/float solution		Positioning Error (meters)			
			Quiet Period (daytime)		Disturbed Period (nighttime)	
	fix	float	HPE	VPE	HPE	VPE
AER1 (4 km)	90.8	9.2	0.0579	0.0759	0.1995	0.4664
STFD (12 km)	68.5	31.5	0.1038	0.1528	1.3154	2.2486
DPT9 (21 km)	46.6	53.4	0.2380	0.17943	3.3514	4.8587

An example of RTK positioning performance during the ionospheric quiet day is shown in Figure 4.4 at 12 km baseline length on DOY001, 2022. On this quiet day, both 95-percent HPE VPE are less than 10 cm with 98 percent fixed rate during daytime and nighttime showing that RTK positioning performance during the quiet nighttime condition has similar accuracy with daytime RTK performance. The positional errors are caused by nominal noise in the system. Therefore, we can say that the disturbed nighttime RTK performance degradation is caused by ionospheric disturbances induced by EPBs.

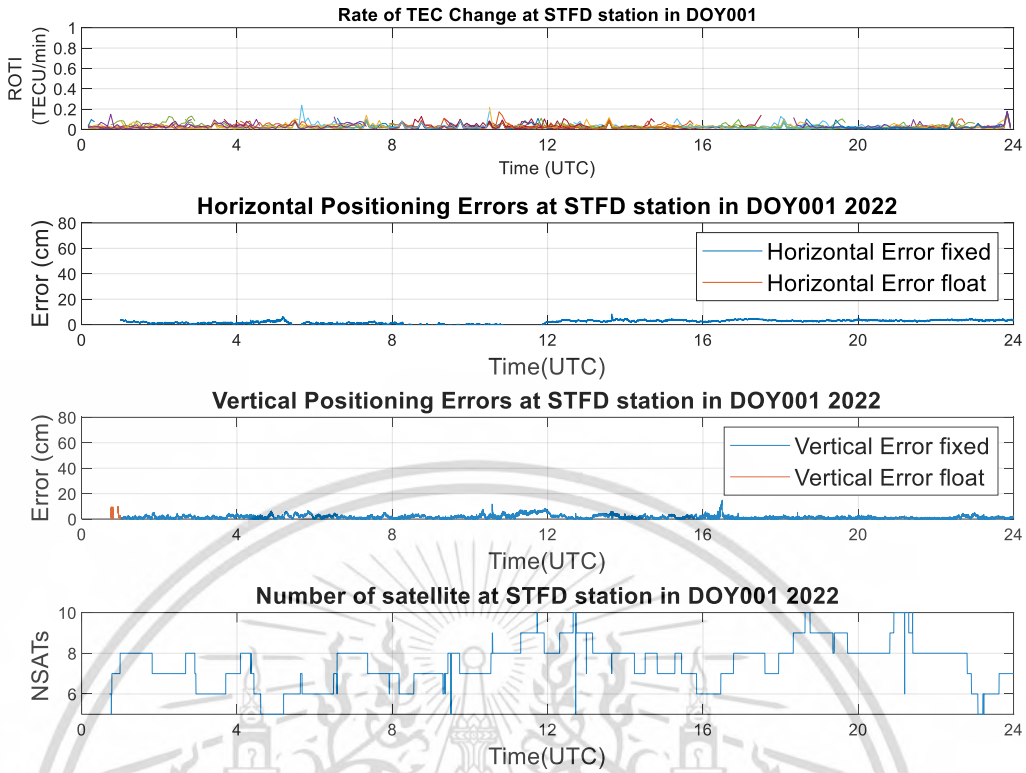

Figure 4.4 Positioning performance during quiet day on DOY001, 2022 at medium baseline

4.1.2 RTK positioning performances at different latitudes over Thailand

Furthermore, we conduct an analysis of RTK positioning performances at various latitudes across Thailand using three GNSS station pairs, as shown in Figure 3.2. For instance, Figure 4.5 demonstrates RTK positioning performances during ionospheric disturbed periods in northern Thailand with a 48 km baseline distance. Similarly, we conduct experiments for RTK positioning in central region of Thailand with a 21 km baseline distance and in the southern region of Thailand region with a 30km baseline distance and the RTK performance are shown in Figure 4.6 and Figure 4.7, respectively. The first column indicates the ROTI of each satellite in different colors. HPE and VPE are presented in the second and third rows, and the number of usable satellites in RTK system are shown in fourth row. It is important to note that obtaining fixed solution proved challenging, with less than 30% of fixed solutions in southern region of Thailand and less than 5% in northern Thailand due to the extensive baseline lengths. In Table 4.2, the 95th percentile positioning errors on DOY 267 of 2022 are summarized. The patterns of positioning errors are consistent across all regions in Thailand, with a significant increase of over 20 times during ionospheric disturbed periods. Notably, errors are higher at longer baseline lengths, reaching up to 30 times compared to the quiet period during the ionospheric disturbed period.

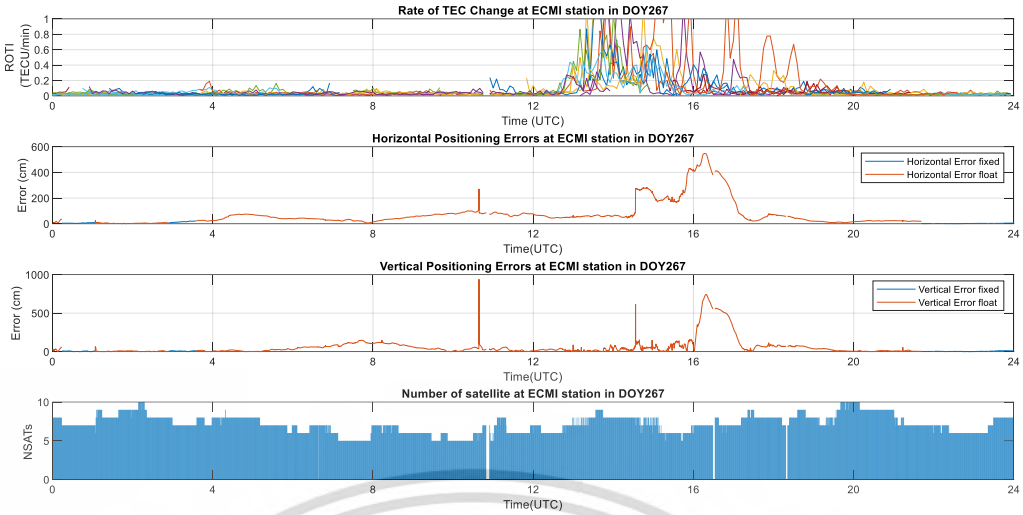

Figure 4.5 Example of RTK positioning performance in Northern Thailand Region on DOY267, 2022.

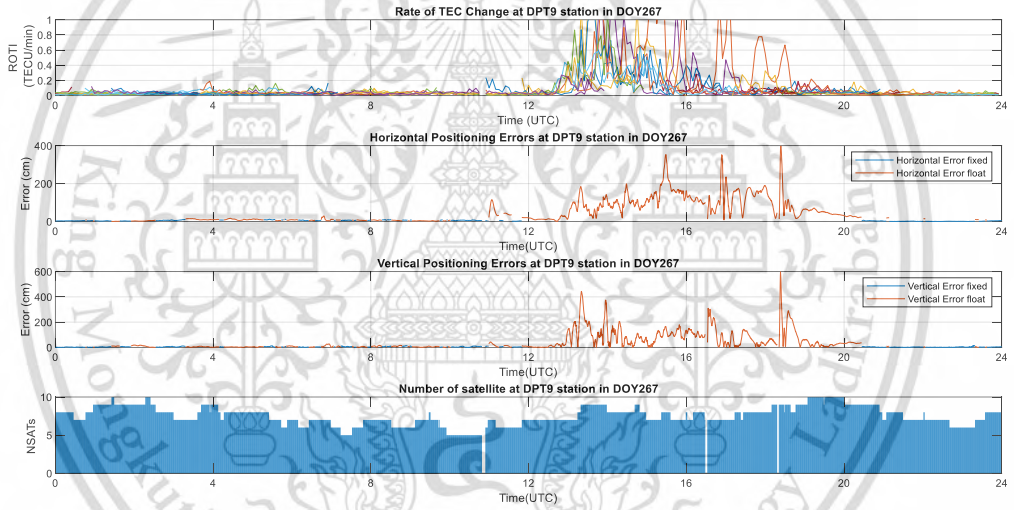

Figure 4.6 Example of RTK positioning performance in Southern Thailand Region on DOY267, 2022.

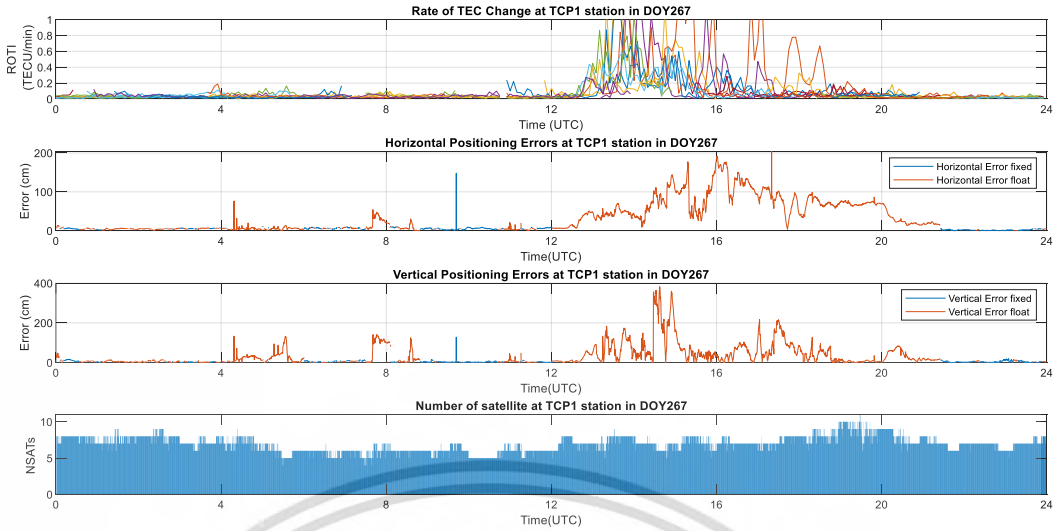

Figure 4.7 Example of RTK positioning performance in Central Thailand Region on DOY267, 2022.

Table 4.2 95-percent positioning error at different latitude regions in Thailand during ionospheric quiet (daytime) and disturbed (nighttime) periods

Baseline length	Percent of fixed/float solution		95-percent Positioning Error (meters)			
			Quiet Period (daytime)		Disturbed Period (nighttime)	
	fixed	float	HPE	VPE	HPE	VPE
ECMI – Northern Thailand (48 km)	9.2	90.8	0.5130	0.8721	4.7126	6.8642
DPT9 - Central Thailand (21 km)	47.9	52.1	0.1940	0.2864	3.3561	3.8587
TCP1 – Southern Thailand (30 km)	37.6	62.4	0.3815	0.5334	3.8971	4.6415

4.1.3 Statistics of RTK positioning errors in 2020 (low solar activity) and in 2022 (high solar activity)

The summary of overall nighttime positioning errors during the disturbed day of 2020 are shown in Figure 4.8 to Figure 4.10 for short baseline, medium baseline, and long baseline, respectively. Similarly, the RTK positioning errors from 2022 are represented in Figure 4.11 to Figure 4.13. In these figures, the first row represents the Kp-index of each day representing the earth's geomagnetic activities. The second row indicates the maximum ROTI of usable satellites in RTK each day. The second to fourth rows describe the maximum and 95-percent RTK positioning errors in each day. Both HPE and VPE demonstrate an increase during ionospheric disturbances, especially around the equinox (color highlighted areas). Longer baseline distances are also associated with high errors in both horizontal and vertical. Notably, 2022 exhibits more high error cases compared to 2020 due to increased geomagnetic activities. Moreover, we observed that higher positioning errors are caused by local ionospheric events rather than global activities for both 2020 and 2022.

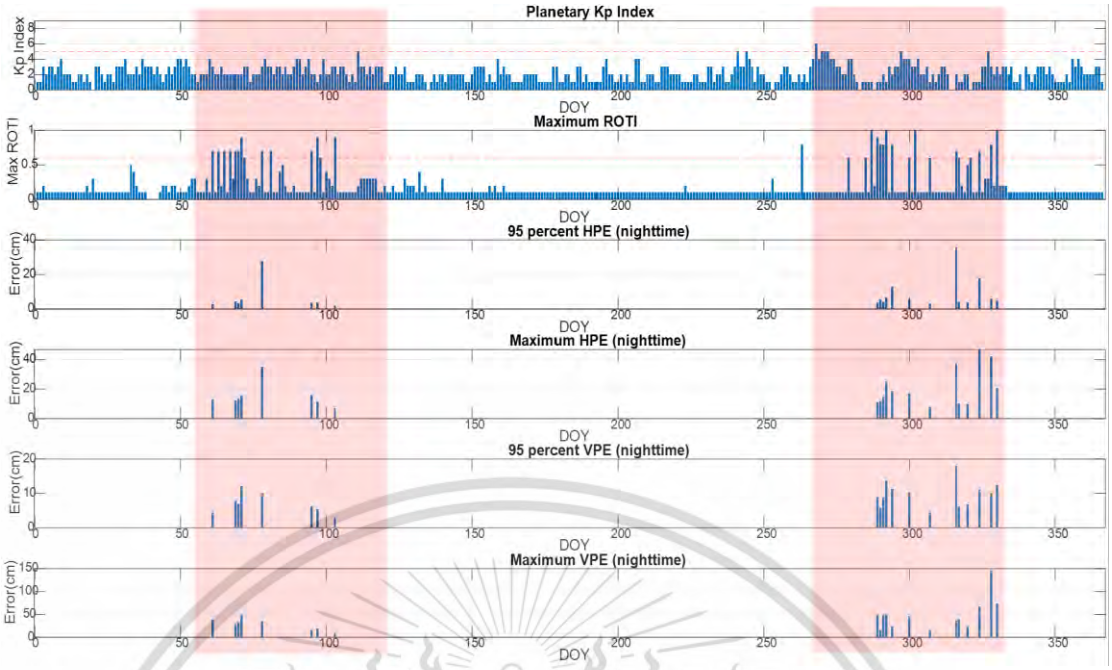

Figure 4.8 Summarized maximum and 95-percent vertical and horizontal positioning errors of 2020 with Kp and ROTI index in short (4 km) baseline.

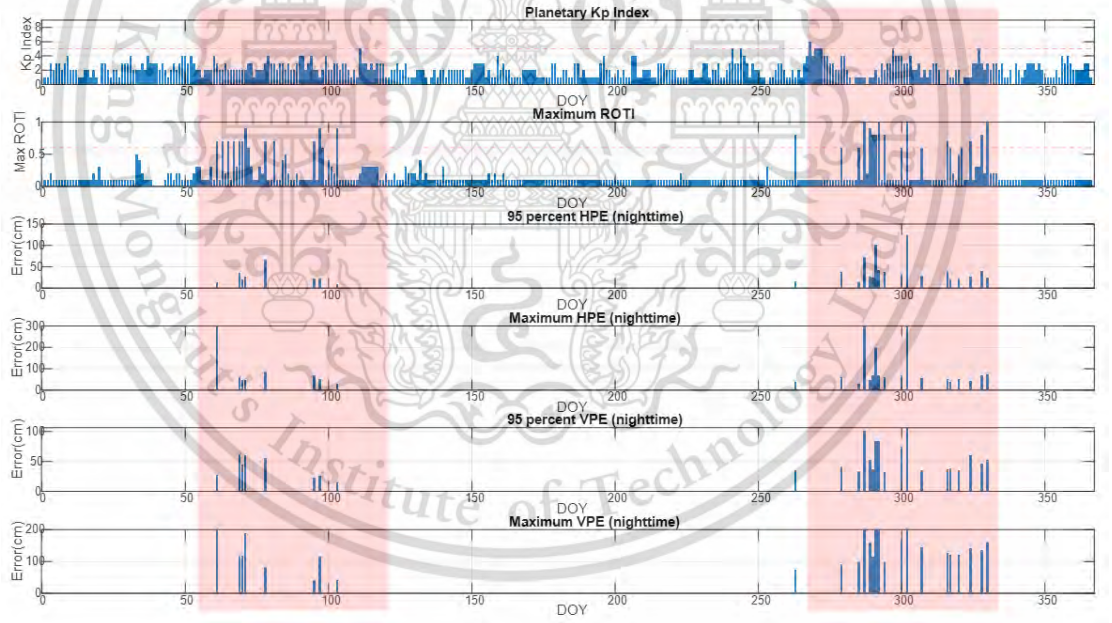

Figure 4.9 Summarized maximum and 95-percent vertical and horizontal positioning errors of 2020 with Kp and ROTI index in short (12 km) baseline.

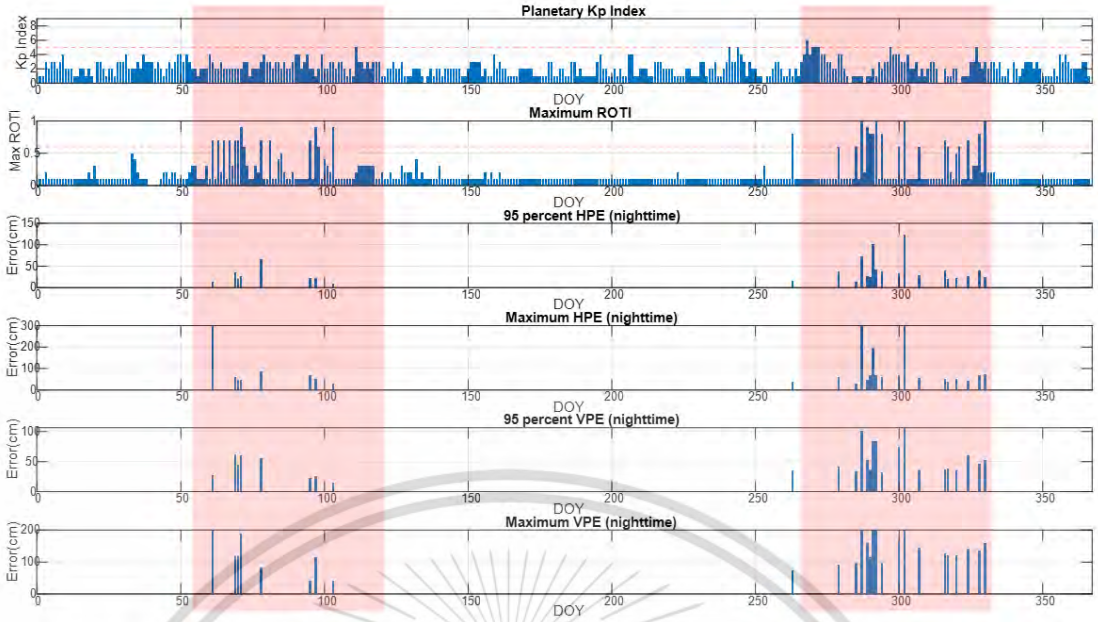

Figure 4.10 Summarized maximum and 95-percent vertical and horizontal positioning errors of 2020 with Kp and ROTI index in short (21 km) baseline.

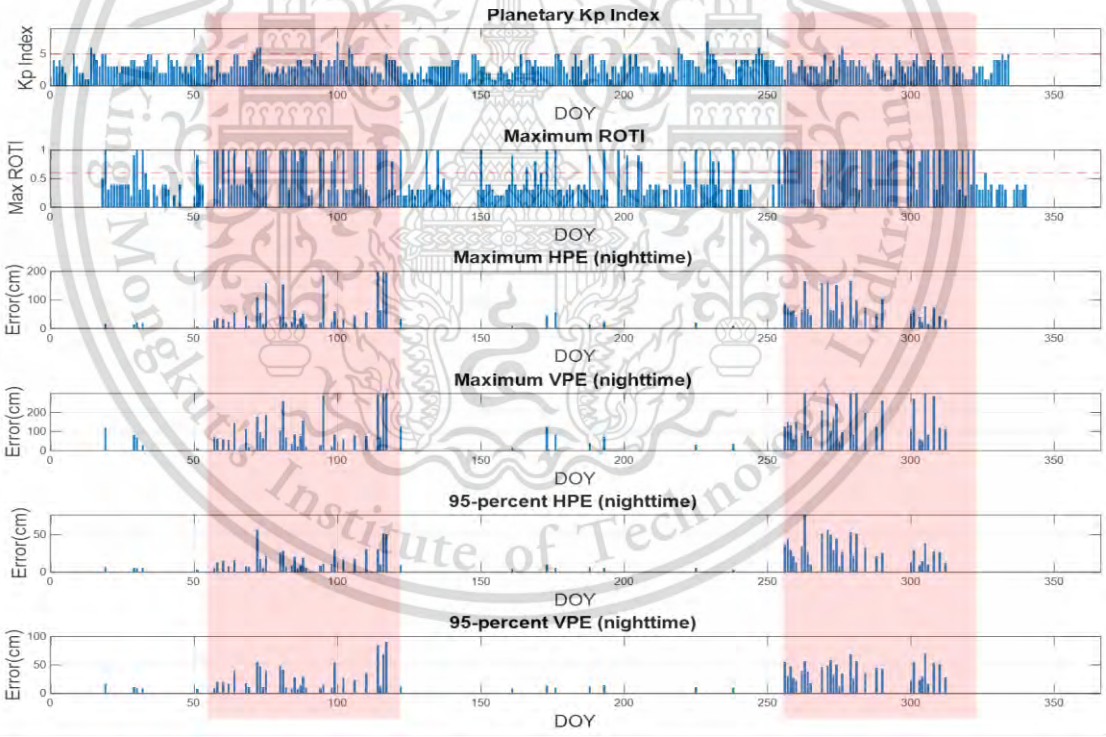

Figure 4.11 Summarized maximum and 95-percent vertical and horizontal positioning errors of 2022 with Kp and ROTI index in short (4 km) baseline.

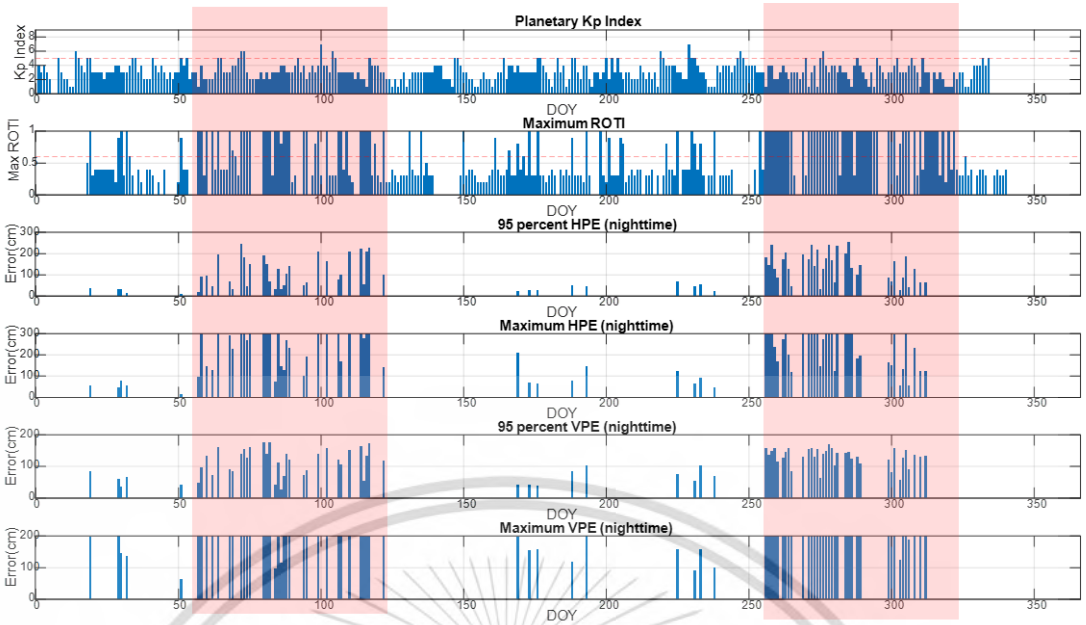

Figure 4.12 Summarized maximum and 95-percent vertical and horizontal positioning errors of 2022 with Kp and ROTI index in short (12 km) baseline.

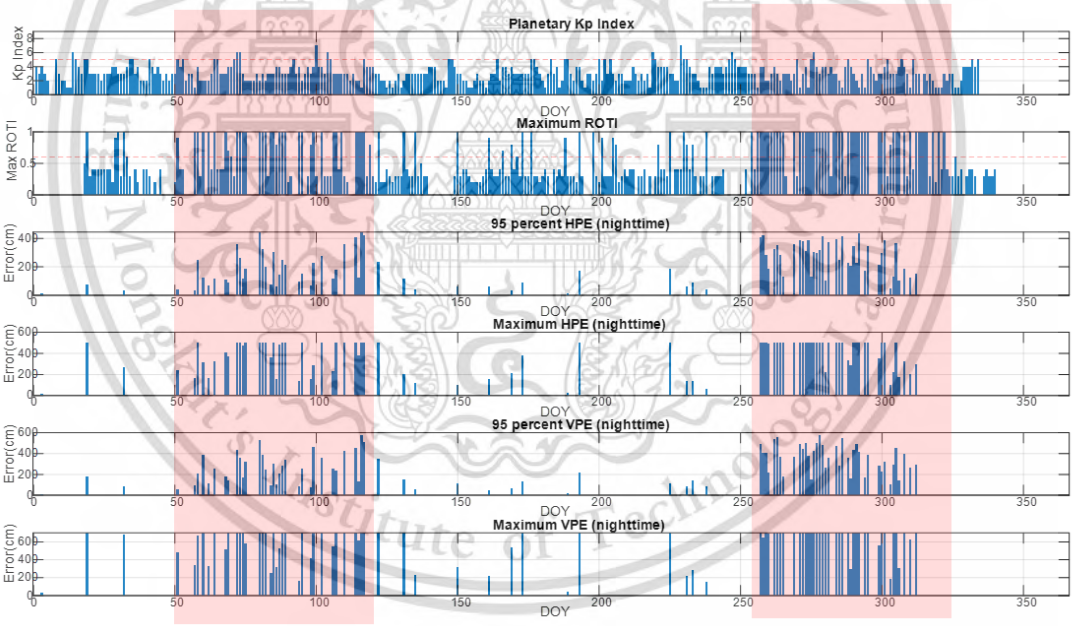

Figure 4.13 Summarized maximum and 95-percent vertical and horizontal positioning errors of 2022 with Kp and ROTI index in short (21 km) baseline.

The box plots in Figure 4.14 (a) and (b) compare the 95-percent positioning errors by RTK during daytime (quiet period with low ROTI) and nighttime (disturbed period with high ROTI) for 2020. Similarly, Figure 4.14 (c) and (d) describe the comparison for 2022. The figures are presented in boxplots where red line indicates the median value and low and upper level of each box represent Q1(25-th percentile) and Q3(750th percentile), respectively. It is evident that both horizontal and vertical errors of all baseline lengths are approximately five times higher during the disturbed

period. Importantly, at longer baseline lengths, errors reach meter-level accuracy (around 4 meters) due to lower percentages of fixed solutions. Furthermore, 2022 exhibits a higher frequency of EPB events during the high solar year, resulting in more cases of enhanced positioning errors compared to 2020.

Figure 4.15 (a) and (b) illustrate the correlation between the maximum ROTI of usable satellites at each epoch and horizontal positioning errors (HPE) and vertical positioning errors (VPE) resulting from the RTK positioning technique. The x-axis indicates the maximum ROTI of usable satellites at each time and the y-axis indicates the horizontal and vertical positioning errors, respectively. The red line represents the correlation between maximum and RTK positioning errors. These observations are made during the period of DOY 305-312 in 2022 when the occurrences of EPBs are detected. The results indicate that horizontal positioning errors increase as ROTI values rise due to significant ionospheric delay variations, which are directly associated with the presence of EPBs.

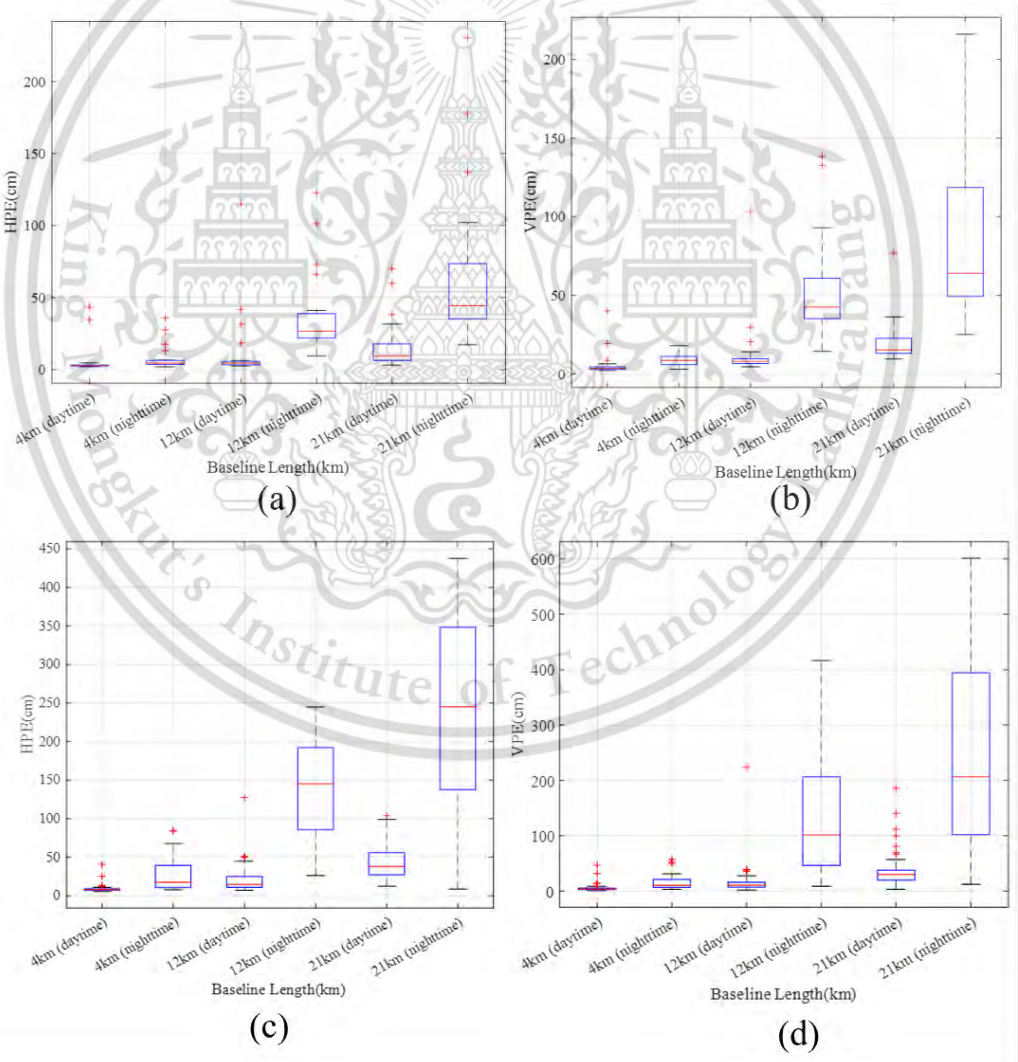

Figure 4.14 95-percent positioning errors by RTK at different baseline lengths in (a) horizontal positioning errors (HPE) in 2020, (b) vertical positioning errors (VPE) in 2020, (c) HPE in 2022, (d) VPE in 2022.

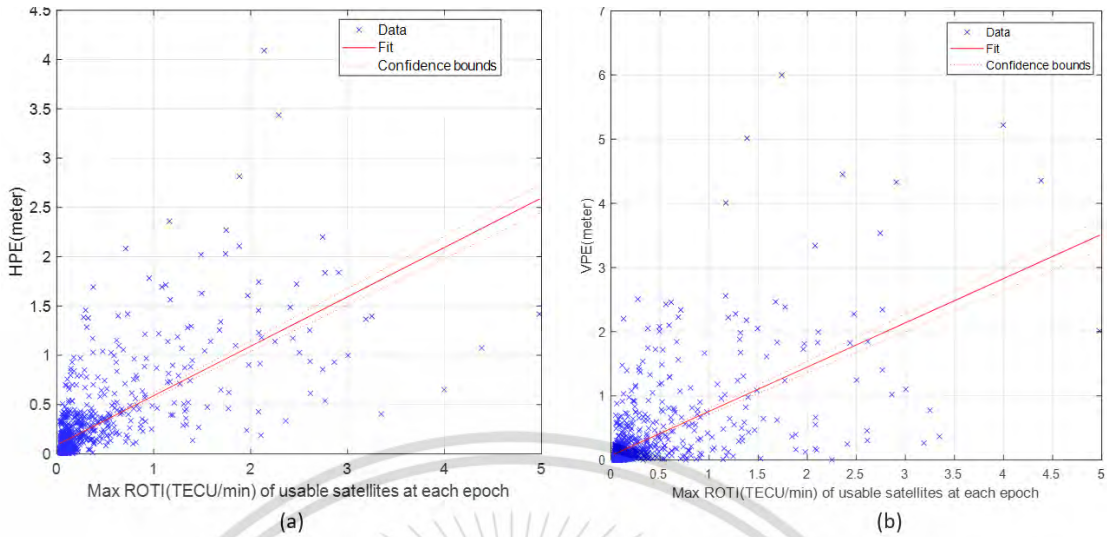

Figure 4.15 Relationship between the maximum ROTI values and (a) horizontal positioning errors (HPE) from RTK in (a) and vertical positioning errors (VPE) from RTK during DOY 305-312, 2022.

4.2 Effects of EPBs on ionospheric delay gradients for GBAS in Thailand region

We analyze the ionospheric delay gradients from observation data of 2021 by using the three stations shown in Figure 3.4. First, we analyze the availably of GPS observation data over three stations and analyze the activity of ionosphere using AATR to determine whether the local ionospheric activities are quite or disturbed in three stations. The summary of availability of data and activity of ionospheric activity are shown in Figure 4.16. 'No Data' means that one of the data from observation data is missing and we cannot compute the delay gradients.

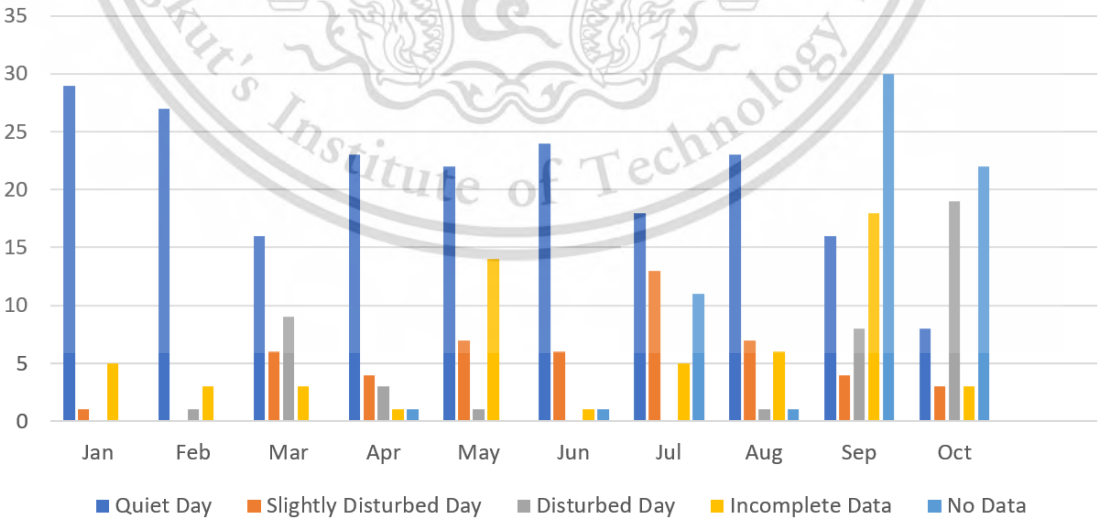

Figure 4.16 Availability of data for ionospheric delay gradients computation and ionospheric activity on 2021.

AATR index is used to determine the ionospheric disturbance by EPBs. The increase or decrease in AATR indicates the ionospheric disturbance. As an example, Figure 4.17 d(a) shows AATR on three stations during quiet day, DOY001, 2021 and Figure 4.17 (b) shows AATR on three stations during disturbed day, DOY300, 2021. The x-axis indicates the GPS time (GPST) which is 7 hours and 18 seconds ahead of local time (LT) in Thailand region. The y-axis indicates the AATR. During quiet ionospheric conditions, AATR is close to zero and fluctuation in AATR typically indicates the occurrence of ionospheric disturbance. The ionospheric disturbances mostly occur during nighttime 12:00 UTC to 18:00 UTC (7:00 p.m. 3:00 am Local Time). If all three stations indicate the abnormal AATR, we consider it as ionospheric disturbances.

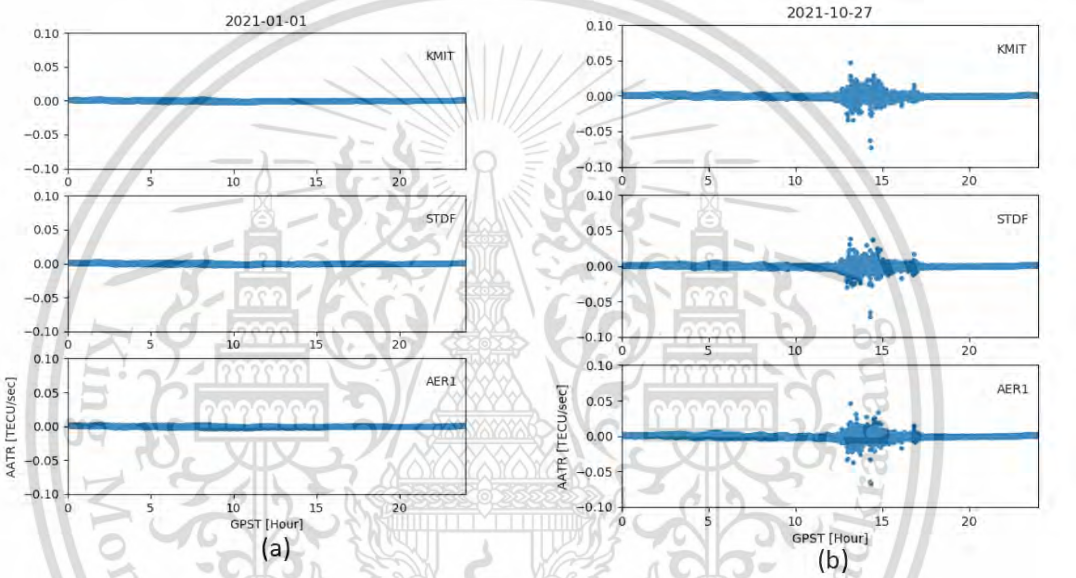

Figure 4.17 AATR during quiet day (a) and during disturbed day (b)

Then, the ionospheric delay gradients are computed using SF-CBCA method as presented in section 2.3.1. The examples of computed ionospheric delay gradients before cyclic sum (consistency check) are shown in Figure 4.18 for quiet day on DOY001, 2021 and in Figure 4.19 for disturbed day on DOY300, 2021. The fist and second rows indicate the ionospheric delay gradient from fixed and float solutions and the third and fourth rows represent the ratio test from LAMDA method.

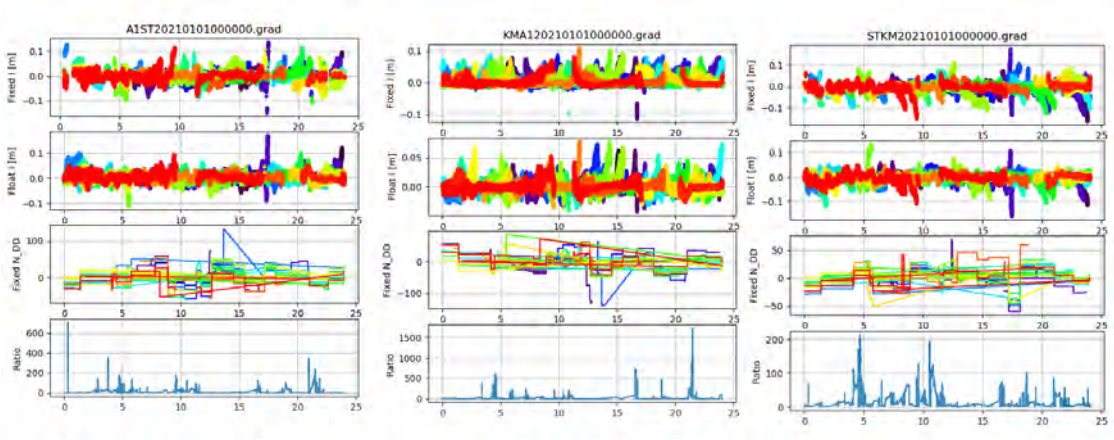

Figure 4.18 Ionospheric delay gradients before cyclic sum during quiet day DOY001, 2021.

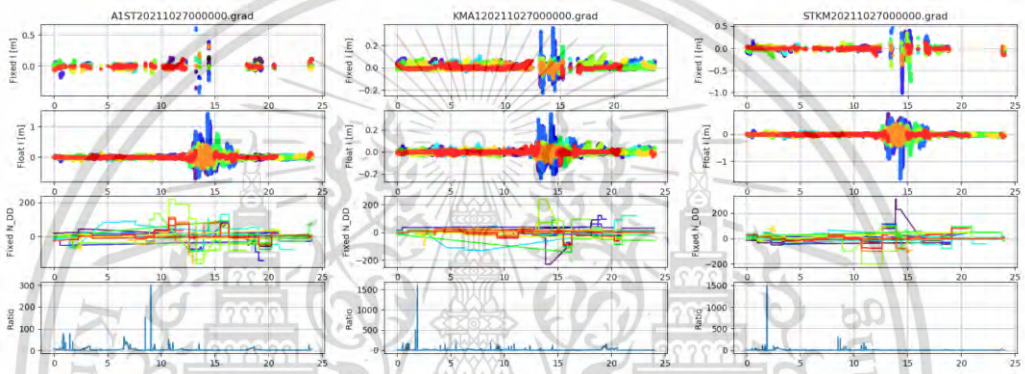

Figure 4.19 Ionospheric delay gradients before cyclic sum during disturbed day DOY300, 2021.

Similarly, the ionospheric delay gradients after cyclic sum (consistency check) are shown in Figure 4.20 (a) as an example of ionospheric delay gradients during quiet day DOY001, 2021, and Figure 4.20 (b) shows an example of ionospheric delay gradients during disturbed day DOY300, 2021. In this case, the East-West gradients are the ionospheric delay gradients between KMIG and STFD stations whereas the North-South gradients are the ionospheric delay gradients between KMIG and AER1 stations where each colors representing different GPS satellites. We can see that the ionospheric delay gradients are significantly large compared to quiet day due to the occurrence of EPB.

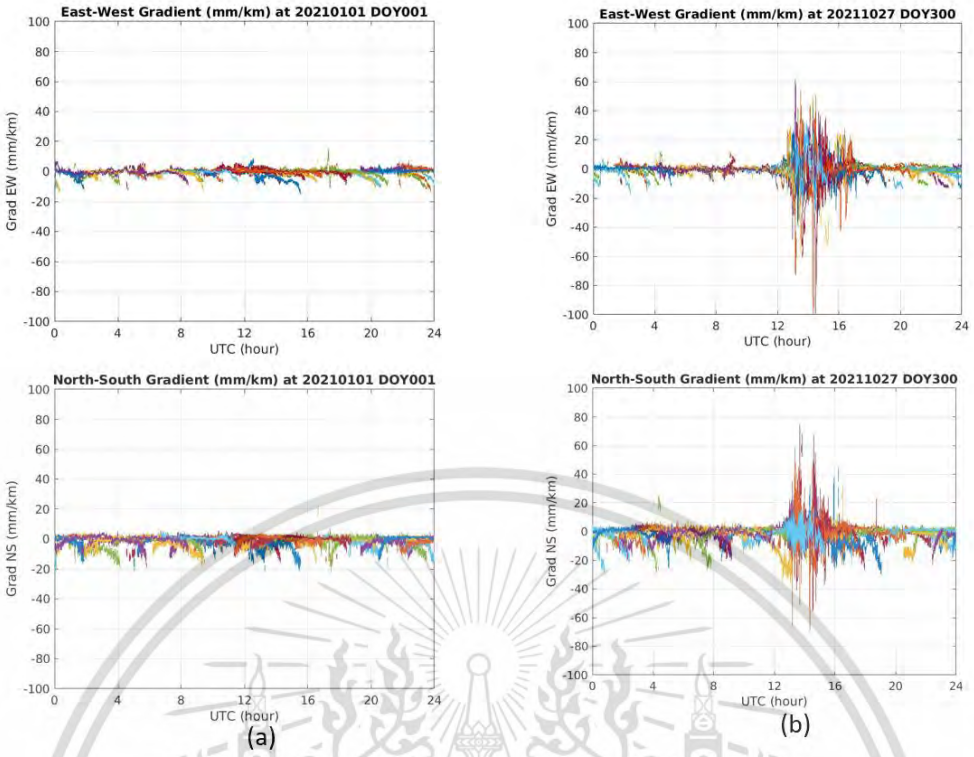

Figure 4.20 Ionospheric delay gradients after cyclic sum during quiet day DOY001,2021 (a), and during disturbed day DOY300, 2021 (b).

The ionospheric delay gradients with respect to AATR during quite day, DOY001, 2021 is shown in Figure 4.21(a) and disturbed day DOY300, 2021 in Figure 4.21(b), respectively. In these figures, the first row represents the AATR which indicates the ionospheric conditions and the second and third rows describe the ionospheric gradients in East-West (EW) and North-South (NS) directions. We can clearly see the increasement of ionospheric delay gradients with the abnormal AATR due to the occurrence of ionospheric disturbances by EPBs.

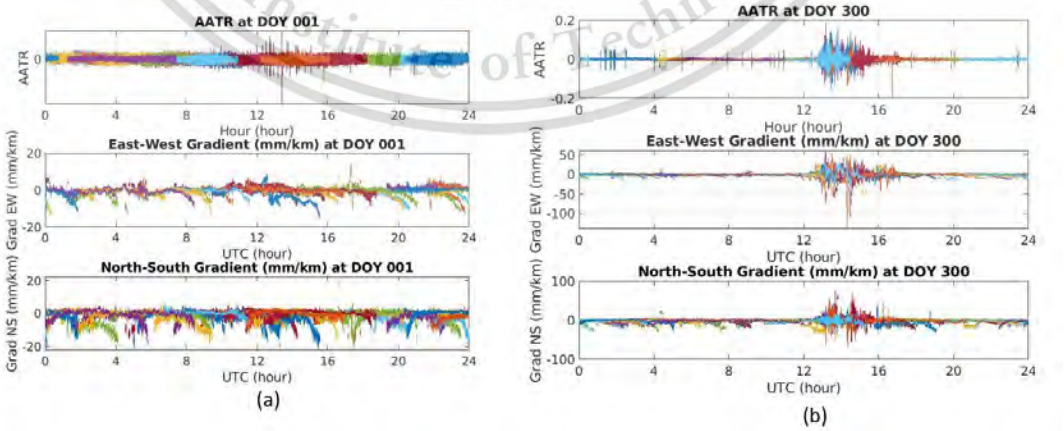

Figure 4.21 Ionospheric delay gradients with respect to AATR during quiet day DOY001, 2021 (a), and during disturbed day DOY300, 2021 (b).

Figure 4.22 shows the ionospheric delay gradients with respect to elevation during quite day, DOY001 2021 in Figure 4.22 (a) and disturbed day DOY300 2021 in Figure 4.22 (b). The x-axis represents the elevation angles of satellites used for ionospheric delay gradient are computed and y-axis presents the ionospheric delay gradient in East-West and North-South direction, respectively. As we can see in Figure 4.22 , ionospheric delay gradients are usually larger at lower elevation angle during ionospheric quiet day. However, the very large ionospheric delay gradients occur at any elevation angle due to the fluctuation of electron density by ionospheric disturbance during disturbed days. So, we can conclude that ionospheric disturbance by EPBs can cause very large ionospheric delay gradients of every effected satellite without elevation angle dependence and have consequence effects on operational capability of GBAS system.

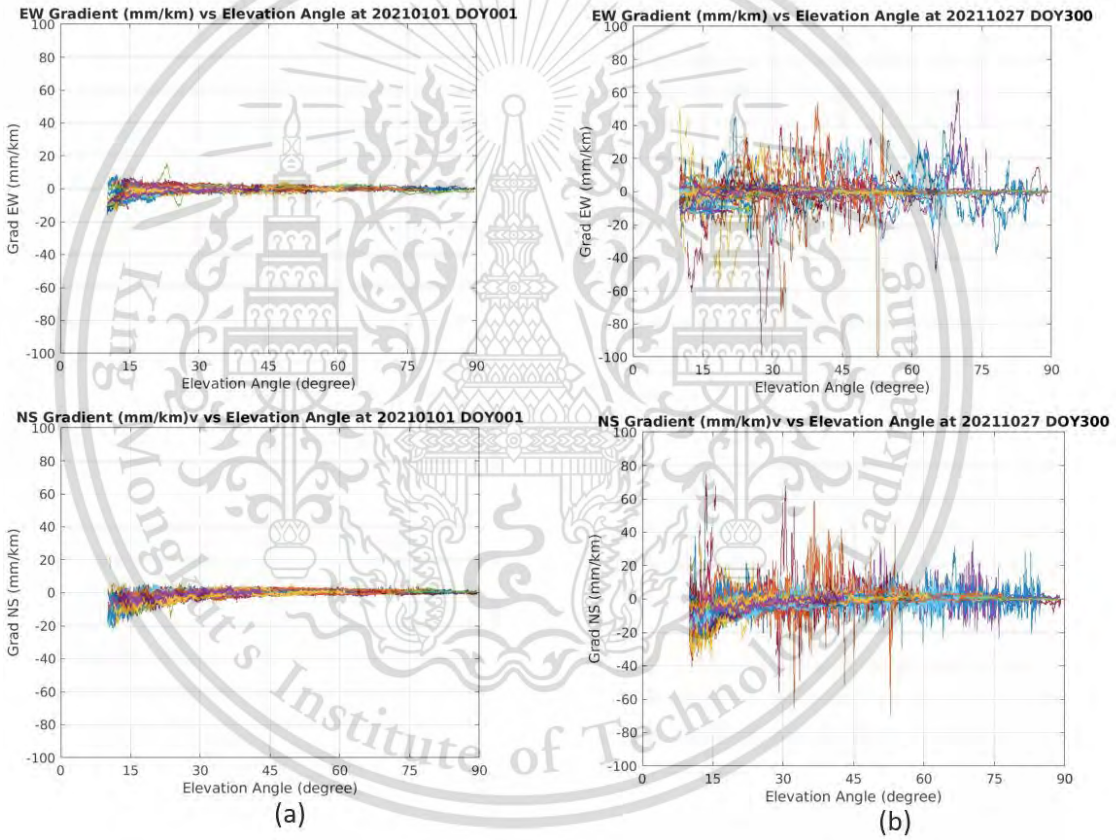

Figure 4.22 Ionospheric delay gradients with respect to elevation angle during quiet day DOY001, 2021 (a), and during disturbed day DOY300, 2021 (b)

4.3 Results of proposed convolutional LSTM model in ionospheric disturbance prediction

Since we observe ionospheric disturbance by EPBs have critical impact on positioning navigation system, monitoring the EPB become important factor. As we discussed in 3.3, we propose

a convolutional LSTM model for prediction of the movement of EPBs to evaluate the feasibility and applicability of machine learning in this area of study. We train our proposed convolutional LSTM model with our pre-process dataset as we discussed in section 3.3.1. The training loss is measured with MSE. The training performance of our proposed model with various numbers of CNN filters and LSTM units is shown in Figure 4.23**.** We select 32 CNN filters with 64 LSTM units for our model after getting the lowest optimal MSE. The training loss of the model with 32 CNN filters with 64 LSTM units is shown in Figure 4.24. We stop the training at 100th epoch after it become converge.

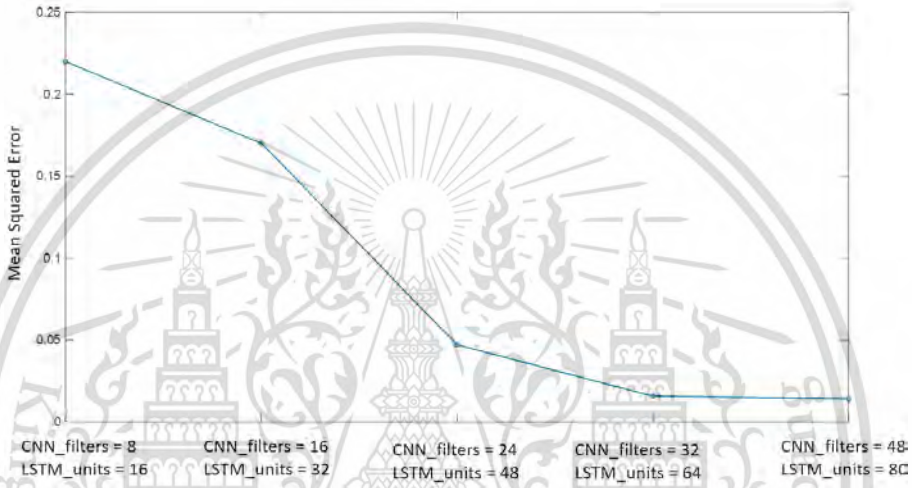

Figure 4.23 Training loss of proposed convolutional LSTM model with different numbers of CNN filters and LSTM units

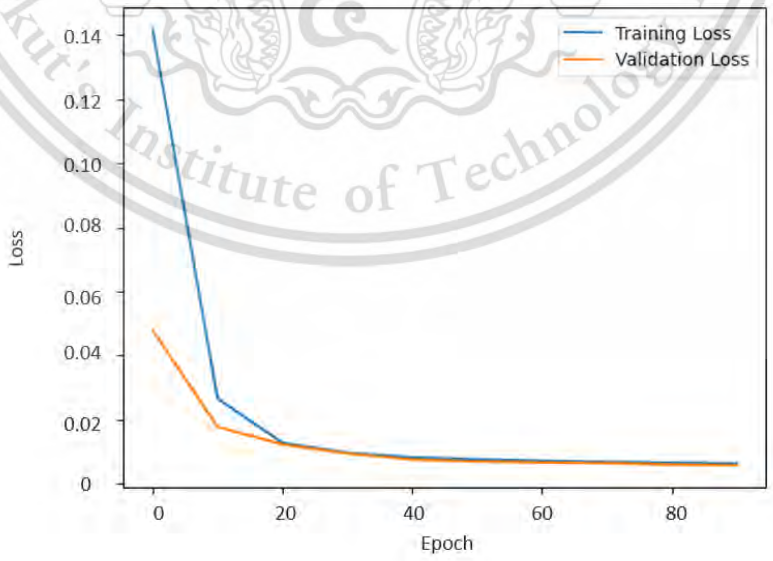

Figure 4.24 Training performance of proposed convolutional LSTM model

After that we evaluate our model with testing dataset. The testing dataset is not part of the training dataset. The comparison of actual frames and predicted frames is shown in Figure 4.25 . The rows show the reference ionospheric ROTI maps computed from actual GNSS observation and the second row present the predicted ionospheric ROTI maps from the proposed convolutional LSTM model in time-series of 25-minutes difference between each frame. We can see the extremely similar characteristic between the actual frame and predicted frame. The performance of the model is evaluated using MSE and SSIM as shown in Table 4.3. As we can see in the table, our proposed model can achieve high accuracy for predicting movement of EPBs and it can predict the structure of the expanding EPB with high similarity. However, the high accuracy seen in the current proposed model might stem from is ability to memorize patterns, especially as EPBs typically follow similar patterns. Consequently, future validation of the model will require more comprehensive and in-depth analysis to address the potential memorization concerns as well to achieve longer prediction capabilities for real-world deployments.

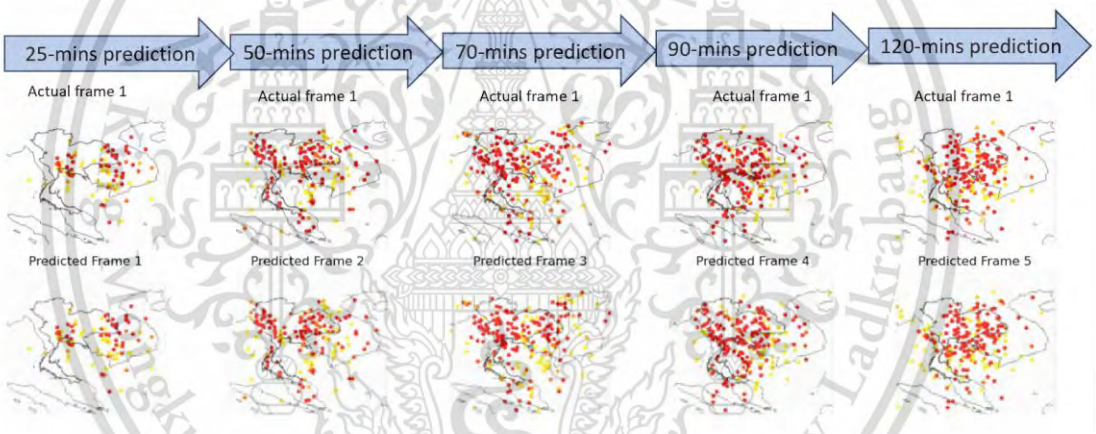

Figure 4.25 Comparison of actual frame from ROTI map and predicted frame from proposed model

Table 4.3 Deviation of actual frames and predicted frames

Evaluation method	Frame1	Frame2	Frame3	Frame4	Frame5
MSE	0.0986	0.1372	0.1406	0.1342	0.1283
SSIM	0.9372	0.9308	0.9385	0.9384	0.9398

Chapter 5 Conclusions and future works

In this thesis, performed three studies. Mainly, we comprehensively analyzed the RTK positioning performances at different baseline distances ranging from 4 to 21km, in a low-latitude region during 2020 (solar minimum) and 2022 (ascending phase to solar maximum) of solar cycle #25. Additionally, we investigated RTK positioning performance across various latitudes of regions within Thailand. The results clearly indicate that positioning errors are significantly large during ionospheric disturbances, with baseline distances playing an important role in exacerbating these errors. Specifically, for long baselines, the expected centimeter-level accuracy of RTK positioning can degrade to the meter-level accuracy. These large positioning errors are notably prevalent during EPB occurrences around the equinox. Moreover, our results highlight a consistent degradation in RTK positioning accuracy across various latitudes in Thailand during disturbed period. We found that the positioning errors escalated with higher ROTI possibly induced by EPBs. Since EPBs can significantly affect the RTK positioning performances in low-latitude regions, we still need to improve the RTK accuracy during the ionospheric disturbed period. Therefore, extensive analysis of mitigation approaches such as monitoring the ionospheric disturbance, removing the effected satellites by EPBs, using local ionospheric parameters for RTK positioning, to increase the performance of RTK positioning during EPB occurrences should be performed in the future.

In addition, we examine the effects of EPBs on ionospheric delay gradients for ground-based augmentation (GBAS) near the Suvarnabhumi International Airport from the observation data of 2021 using SF-CBCA method. We have observed that the EPB can lead to significantly large ionospheric gradients in satellite signals across all elevation angles during disturbed times, in contrast to the occurrence of low to moderate delay gradients from high to low elevation angles. Since EPBs can cause very large ionospheric gradients and consequently affecting the availability of GBAS, ionospheric front monitoring and mitigation approaches of ionospheric disturbance effects such as DFMC-GBAS should be studied at low-latitude regions in the future.

Moreover, we have conducted an investigation into the potential and utility of machine learning approach for predicting the ionospheric disturbances in low-latitude regions. We propose the use of a convolutional long short-term memory (LSTM) model with a next-frame prediction approach, utilizing ionospheric Rate of TEC Index (ROTI) maps of the Thailand region to predict the movement of EPBs. The results of our proposed model demonstrate its effectiveness and feasibility in predicting EPBs with relatively low errors. However, further experiments and studies are required to refine and validate these findings. It is recommended to use the interpolated Rate of TEC Index (ROTI) maps into the convolutional LSTM model for detection, tracking and prediction of EPBs in future studies. Furthermore, there is a necessity to establish a prediction model for Equatorial Plasma Bubbles (EPBs) occurrence by amalgamating local and global ionospheric data in the future.

Real-time reliable warning of affected satellites by EPBs using machine learning should also be considered to mitigate the impact of EPBs over navigation and positioning systems.

REFERENCES

[1] S. Saito et al., "Ionospheric delay gradient model for GBAS in the Asia-Pacific region," *GPS Solutions*, vol. 21, no. 4, 2017.

[2] M. Karaim, M. Elsheikh, and A. Noureldin, "GNSS error sources," in *Multifunctional Operation and Application of GPS*, 2018.

[3] K. S. Jacobsen and M. Dähnn, "Statistics of ionospheric disturbances and their correlation with GNSS positioning errors at high latitudes," *Journal of Space Weather and Space Climate*, vol. 4, 2014.

[4] J. A. Klobuchar, "Ionospheric time-delay algorithm for single-frequency GPS users," *IEEE Transactions on Aerospace and Electronic Systems*, vol. AES-23, no. 3, 1987.

[5] X. Wu, X. Hu, G. Wang, H. Zhong, and C. Tang, "Evaluation of COMPASS ionospheric model in GNSS positioning," *Advances in Space Research*, vol. 51, no. 6, 2013.

[6] A. Rovira-Garcia, J. M. Juan, J. Sanz, G. González-Casado, and D. Ibáñez, "Accuracy of ionospheric models used in GNSS and SBAS: methodology and analysis," *Journal of Geodesy*, vol. 90, no. 3, 2016.

[7] D. Odijk, "Ionosphere-free phase combinations for modernized GPS," *Journal of Surveying Engineering*, vol. 129, no. 4, 2003.

[8] S. Yu and Z. Liu, "The ionospheric condition and GPS positioning performance during the 2013 tropical cyclone Usagi event in the Hong Kong region," *Earth, Planets and Space*, vol. 73, no. 1, 2021.

[9] H. Kil, "The morphology of equatorial plasma bubbles - a review," *Journal of Astronomy and Space Sciences*, vol. 32, no. 1. 2015.

[10] D. Okoh et al., "Equatorial plasma bubble intensities across longitudinal sectors of the globe using GNSS observations," *Journal of Atmospheric and Solar-Terrestrial Physics*, vol. 249, 2023.

[11] L. C. Sun, J. Y. Xu, Y. J. Zhu, W. Yuan, and X. K. Zhao, "Case study of an Equatorial Plasma Bubble Event investigated by multiple ground-based instruments at low latitudes over China," *Earth and Planetary Physics*, vol. 5, no. 5, 2021.

[12] A. de O. Moraes et al., "GPS availability and positioning issues when the signal paths are aligned with ionospheric plasma bubbles," *GPS Solutions*, vol. 22, no. 4, 2018.

[13] S. Tulasi Ram, K. K. Ajith, T. Yokoyama, M. Yamamoto, and K. Niranjan, "Vertical rise velocity of equatorial plasma bubbles estimated from Equatorial Atmosphere Radar (EAR) observations and HIRB model simulations," *Journal of Geophysical Research: Space Physics*, vol. 122, no. 6, 2017.

[14] Paziewski Jacek et al., "The implications of ionospheric disturbances for precise GNSS positioning in Greenland," *Journal of Space Weather and Space Climate*, vol. 12, p. 33, 2022.

[15] Z. Yang, Y. T. J. Morton, I. Zakharenkova, I. Cherniak, S. Song, and W. Li, "Global view of ionospheric disturbance impacts on kinematic GPS positioning solutions during the 2015 St. Patrick's Day storm," *Journal of Geophysical Research: Space Physics*, vol. 125, no. 7, 2020.

[16] K. S. Jacobsen and S. Schäfer, "Observed effects of a geomagnetic storm on an RTK positioning network at high latitudes," *Journal of Space Weather and Space Climate*, vol. 2, 2012.

[17] I. Zakharenkova and I. Cherniak, "Effects of storm-induced equatorial plasma bubbles on GPS-based kinematic positioning at equatorial and middle latitudes during the September 7–8, 2017, geomagnetic storm," *GPS Solutions*, vol. 25, no. 4, 2021.

[18] K. Guo, M. Aquino, S. V. Veettil, Z. Liu, W. Chen, and H. A. Marques, "Analysis of ionospheric scintillation and its impact on PPP at low latitudes," in *Proceedings of the Institute of Navigation Pacific Positioning, Navigation and Timing Meeting, Pacific PNT*, 2019, vol. 2019-April.

[19] Y. Ning and J. Tang, "Study of ionospheric disturbances over the China mid- and low-latitude region with GPS observations," *Annales Geophysicae*, vol. 36, no. 1, 2018.

[20] W. Li, S. Song, W. Zhou, N. Cheng, and C. Yu, "Investigating the impacts of ionospheric irregularities on precise point positioning over China and its mechanism," *Space Weather*, vol. 20, no. 11, 2022.

[21] T. Dautermann, M. Felux, and A. Grosch, "Approach service type D evaluation of the DLR GBAS testbed," *GPS Solutions*, vol. 16, no. 3, 2012.

[22] H. Konno, S. Pullen, M. Luo, and P. Enge, "Analysis of ionosphere gradient using Japan GEONET data," in *Proceedings of the Institute of Navigation, National Technical Meeting*, 2005.

[23] S. Shi et al., "An Investigation of ionospheric TEC prediction maps over China using bidirectional Long Short-Term Memory method," *Space Weather*, vol. 20, no. 6, p. e2022SW003103, 2022.

[24] S. A. Reddy et al., "Predicting swarm equatorial plasma bubbles via machine learning and shapley values," *Journal of Geophysical Research: Space Physics*, vol. 128, no. 6, 2023.

[25] L. Liu, Y. J. Morton, and Y. Liu, "Machine learning prediction of storm-time high-latitude ionospheric irregularities from GNSS-derived ROTI maps," *Geophysical Research Letters*, vol. 48, no. 20, p. e2021GL095561, 2021.

[26] L. B. Liu, W. X. Wan, Y. D. Chen, and H. J. Le, "Solar activity effects of the ionosphere: A brief review," *Chinese Science Bulletin*, vol. 56, no. 12. 2011.

[27] M. C. Kelley, "Equatorial plasma instabilities," The Earth's Ionosphere, pp. 113–185, Jan. 1989.

[28] R. A. Heelis, R. Stoneback, G. D. Earle, R. A. Haaser, and M. A. Abdu, "Medium-scale equatorial plasma irregularities observed by Coupled Ion-Neutral Dynamics Investigation sensors aboard the Communication Navigation Outage Forecast System in a prolonged solar minimum," *Journal of Geophysical Research: Space Physics*, vol. 115, no. 10, 2010.

[29] R. F. Woodman and C. La Hoz, "Radar observations of F region equatorial irregularities," *Journal of Geophysical Research*, vol. 81, no. 31, 1976.

[30] A. Bumrungkit, P. Supnithi, S. Saito, and L. M. M. Myint, “A study of equatorial plasma bubble structure using VHF radar and GNSS scintillations over the low-latitude regions,” *GPS Solutions*, vol. 26, no. 4, 2022.

[31] H. Tuna, O. Arikan, F. Arikan, T. L. Gulyaeva, and U. Sezen, “Online user-friendly slant total electron content computation from IRI-Plas: IRI-Plas-STEC,” *Space Weather*, vol. 12, no. 1, 2014.

[32] G. Ma and T. Maruyama, “Derivation of TEC and estimation of instrumental biases from GEONET in Japan,” *Annales Geophysicae*, vol. 21, no. 10, 2003.

[33] D. R. Themens, P. T. Jayachandran, and R. B. Langley, “The nature of GPS differential receiver bias variability: An examination in the polar cap region,” *Journal of Geophysical Research A: Space Physics*, vol. 120, no. 9, 2015.

[34] G. Ma and T. Maruyama, “Derivation of TEC and estimation of instrumental biases from GEONET in Japan,” *Annales Geophysicae*, vol. 21, no. 10, 2003.

[35] International Association of Geodesy, “International GNSS Service,” Jul. 2022.

[36] A. Chiablaem et al., “Estimation of the single GPS-receiver bias using the gradient descent algorithm,” in *2016 13th International Conference on Electrical Engineering/Electronics, Computer, Telecommunications and Information Technology, ECTI-CON 2016*, 2016.

[37] X. Pi, A. J. Mannucci, U. J. Lindqwister, and C. M. Ho, “Monitoring of global ionospheric irregularities using the worldwide GPS network,” *Geophysical Research Letter*, vol. 24, no. 18, 1997.

[38] J. M. Juan, J. Sanz, A. Rovira-Garcia, G. González-Casado, D. Ibáñez, and R. O. Perez, “AATR an ionospheric activity indicator specifically based on GNSS measurements,” *Journal of Space Weather and Space Climate*, vol. 8, 2018.

[39] J. Matzka, C. Stolle, Y. Yamazaki, O. Bronkalla, and A. Morschhauser, “The geomagnetic Kp index and derived indices of geomagnetic activity,” *Space Weather*, vol. 19, no. 5, 2021.

[40] Parsec vzw, “SpaceWeatherLive.” https://www.spaceweatherlive.com/ (accessed May 10, 2023).

[41] Kyoto University, “Geomagnetic equatorial Dst index home page.” https://wdc.kugi.kyoto-u.ac.jp/dstdir/ (accessed May 10, 2023).

[42] M. El-Eraki, A. Lethy, A. Samy, and H. Deebes, “The disturbance storm time (Dst) index prediction using time delay neural network during some extreme geomagnetic storms.” 2018.

[43] H. He, J. Li, Y. Yang, J. Xu, H. Guo, and A. Wang, “Performance assessment of single- and dual-frequency BeiDou/GPS single-epoch kinematic positioning,” *GPS Solutions*, vol. 18, no. 3, 2014.

[44] Y. Huang, J. Fu, S. Xu, T. Han, and Y. Liu, “Research on integrated navigation system of agricultural machinery based on RTK-BDS/INS,” *Agriculture (Switzerland)*, vol. 12, no. 8, 2022.

[45] H. Xu, “Application of GPS-RTK technology in the land change survey,” in *Procedia Engineering*, 2012, vol. 29.

[46] T. Takasu, RTKLIB ver. 2.4.2 Manual. 2013.

[47] C. C. Robusto, “The Cosine-Haversine formula,” *The American Mathematical Monthly*, vol. 64, no. 1, 1957.

[48] International Civil Aviation Organization, *International standards and recommended practices. Annex 10 to the Convention on the International Civil Aviation, Amendment 89*. 2014.

[49] S. Gleason and D.-E. Gebre, *GNSS Applications and Methods*. 2015.

[50] M. Mendillo, “Storms in the ionosphere: Patterns and processes for total electron content,” *Reviews of Geophysics*, vol. 44, no. 4. 2006.

[51] S. Saito, T. Yoshihara, and S. Fujita, “Absolute gradient monitoring for GAST-D with a single-frequency carrier-phase based and code- aided technique,” in *25th International Technical Meeting of the Satellite Division of the Institute of Navigation 2012, ION GNSS 2012*, 2012, vol. 3.

[52] S. Fujita, T. Yoshihara, and S. Saito, “Determination of ionosphere gradient in short baselines by using single frequency measurements,” *Journal of Aeronautics, Astronautics and Aviation*, vol. 42, no. 4, 2010.

[53] J. Budtho, P. Supnithi, A. Saekow, and S. Saito, “Nominal ionospheric delay gradient estimation at Suvarnabhumi airport, Thailand,” in *2017 International Electrical Engineering Congress, iEECON 2017*, 2017.

[54] S. Saito, S. Fujita, and T. Yoshihara, “Precise measurements of ionospheric delay gradient at short baselines associated with low latitude ionospheric disturbances,” in *Institute of Navigation International Technical Meeting 2012, ITM 2012*, 2012, vol. 2.

[55] J. Budtho, P. Supnithi, and S. Saito, “Analysis of quiet time vertical ionospheric delay gradients around Suvarnabhumi airport, Thailand,” *Radio Science*, vol. 53, no. 9, pp. 1067–1074, Sep. 2018.

[56] A. Brack, “Long baseline GPS+BDS RTK positioning with partial ambiguity resolution,” in *Proceedings of the 2017 International Technical Meeting of The Institute of Navigation, ITM 2017*, 2017.

[57] P. Thammavongsy, P. Supnithi, L. M. M. Myint, K. Hozumi, and D. Lakanchanh, “Equatorial spread-F forecasting model with local factors using the long short-term memory network,” *Earth, Planets and Space*, vol. 75, no. 1, p. 118, Aug. 2023.

[58] K. Watthanasangmechai, P. Supnithi, S. Lerkvaranyu, T. Tsugawa, T. Nagatsuma, and T. Maruyama, “TEC prediction with neural network for equatorial latitude station in Thailand,” *Earth, Planets and Space*, vol. 64, no. 6, 2012.

[59] S. Sahu, R. Trivedi, R. K. Choudhary, A. Jain, and S. Jain, “Prediction of Total Electron Content (TEC) using Neural Network over Anomaly Crest Region Bhopal,” *Advances in Space Research*, vol. 68, no. 7, 2021.

[60] D. Balderas, P. Ponce, and A. Molina, “Convolutional long short term memory deep neural networks for image sequence prediction,” *Expert Systems with Applications*, vol. 122, pp. 152–162, May 2019.

[61] P. Kumari and D. Toshniwal, "Long short term memory–convolutional neural network based deep hybrid approach for solar irradiance forecasting," *Applied Energy*, vol. 295, p. 117061, Aug. 2021.

[62] L. Liu, Y. J. Morton, and Y. Liu, "Machine learning prediction of storm-time high-latitude ionospheric irregularities from GNSS-derived ROTI maps," *Geophysical Research Letter*, vol. 48, no. 20, Oct. 2021.

[63] A. F. Siegel and M. R. Wagner, "Statistical (machine) learning," in *Practical Business Statistics*, Elsevier, 2022, pp. 571–599.

[64] P. Thammavongsy, P. Supnithi, L. M. M. Myint, K. Hozumi, and D. Lakanchanh, "Equatorial spread-F forecasting model with local factors using the long short-term memory network," *Earth, Planets and Space*, vol. 75, no. 1, p. 118, Aug. 2023.

[65] J. Weng, Y. Liu, and J. Wang, "A model-assisted combined machine learning method for ionospheric TEC prediction," *Remote Sensing (Basel)*, vol. 15, no. 12, p. 2953, Jun. 2023.

[66] GFZ Potsdam, "GFZ German research center for geoscience." https://www.gfz-potsdam.de/en/ (accessed May 10, 2023).

[67] AUSPOS, "Online GPS processing service," https://www.ga.gov.au/scientific-topics/positioning-navigation/geodesy/auspos.

APPENDIX

Lists of Conference/Journal Publications

- P. C. Thu, P. Supnithi, L. M. Min Myint, S. Saito, A. Saekow and K. Hozumi, "Neural Network Prediction of Receiver Bias in Ionospheric Delay Computation," 2022 19th International Conference on Electrical Engineering/Electronics, Computer, Telecommunications and Information Technology (ECTI-CON), HauHin, Thailand, May 2022.
- P. C. Thu, P. Supnithi, L. M. Min Myint, J. Budtho, S. Saito, A, Saekow and N. Sianawasdi, "Study on the effect of Equatorial Plasma Bubble over Real-Time Kinematic Positioning in Bangkok Thailand," 2022 37th International Technical Conference on Circuits/Systems, Computers and Communications (ITC-CSCC), Phuket, Thailand, June 2022.
- P. C. Thu, P. Supnithi, L. M. Min Myint, J. Budtho, S. Saito, A. Saekow, T. Sopon and K. Hozumi, " Instrumental Receiver Bias Estimation for Ionospheric Total Electron Content by Neural Network Model," The ECTI Transactions on Electrical Engineering, Electronics, and Communications (ECTI-EEC).
- P. C. Thu, P. Supnithi, L. M. Min Myint, and J. Budtho, “Effects of Equatorial Plasma Bubbles on RTK Positioning in Low-latitude region” ION GNSS+ 2023, Coloraldo, USA.